AGU PUBLICATIONS

JGR

Journal of Geophysical Research: Oceans

RESEARCH ARTICLE

10.1002/2015JC010860

Characterizing the circulation off the Kenyan-Tanzanian coast using an ocean model

C. Gabriela Mayorga-Adame[1], P. Ted Strub[1], Harold P. Batchelder[2], and Yvette H. Spitz[1]

[1]College of Ocean and Atmospheric Sciences, Oregon State University, Corvallis, Oregon, USA, [2]North Pacific Marine Science Organization, Sidney, British Columbia, Canada

Key Points:
- The 4 km resolution Kenyan-Tanzanian ocean model reproduce main circulation features
- Model reveals two shelf circulation regimes: retentive and strong northward flow
- Model provide details of coastal circulation, i.e., small eddies

Supporting Information:
- Supporting Information S1

Correspondence to:
C. G. Mayorga-Adame,
cmayorga@coas.oregonstate.edu

Citation:
Mayorga-Adame, C. G., P. T. Ted Strub, H. P. Batchelder, and Y. H. Spitz (2016), Characterizing the circulation off the Kenyan-Tanzanian coast using an ocean model, *J. Geophys. Res. Oceans*, *121*, 1377–1399, doi:10.1002/2015JC010860.

Received 20 MAR 2015
Accepted 6 JAN 2016
Accepted article online 12 JAN 2016
Published online 18 FEB 2016

Abstract The Kenyan-Tanzanian coastal region in the western Indian Ocean faces several environmental challenges including coral reef conservation, fisheries management, coastal erosion, and nearshore pollution. The region lacks hydrodynamic records and oceanographic studies at adequate spatial and temporal scales to provide information relevant to the local environmental issues. We have developed a 4 km horizontal resolution ocean circulation model of the region: the Kenyan-Tanzanian Coastal Model (KTCM) that provides coastal circulation and hydrography with higher resolution than previous models and observational studies of this region. Comparisons to temperature profiles, satellite-derived sea surface temperature and sea surface height anomaly fields, indicate that the model reproduces the main features of the regional circulation, while greatly increasing the details of the nearshore circulation. We describe the seasonal ocean circulation and hydrography of the Kenyan-Tanzanian coastal region based on a climatology of 8 years (2000–2007) of the KTCM simulations. The regional monsoon seasonality produces two distinct coastal circulation regimes: (1) during December–March, there are relatively sluggish shelf flows and (2) during April–November, there are strong northward transports. Simulations from the model will be useful for examining dispersal of pollutants and spatial connectivity of coral reef species.

1. Introduction

Fishing, mangrove exploitation, tourism, and harbor services are important to the economies of Kenya and Tanzania. Approximately, 20% of the gross domestic income of these countries is derived directly or indirectly from the coastal economies. Inadequate management of the marine resources has resulted in overexploitation, habitat destruction, pollution, and coastal erosion that diminish the value of coastal resources and activities [*Odido and Mazzilli*, 2009; *Payet and Obura*, 2004; *Richmond*, 1997]. A better understanding of the ocean circulation at temporal and spatial resolutions appropriate to these environmental issues will be valuable. However, this part of the East African coastal ocean has been grossly undersampled in comparison to neighboring areas such as the Somali coast and the Arabian Gulf [e.g., *Vimal Kumar et al*., 2008; *Smith et al*., 1998], the Red Sea [e.g., *Roman and Lutjeharms*, 2009], and the Mozambique Channel [e.g., *van der Werf et al*., 2010; *Ridderinkhof et al*., 2010; *da Silva et al*., 2009; *Nauw et al*., 2008; *Matano et al*., 2002]. Historically, the undersampling is due to economical constraints of the local countries and the remoteness of the region, far from major oceanographic research institutes. Observational studies in the Kenyan-Tanzanian region continue to be a challenge, since most ships, including oceanographic research vessels, avoid the area due to concerns about piracy and high insurance expenses [*Bendekovic and Vuletic*, 2013].

Our knowledge of coastal dynamics off East Africa is based on limited observations [*Manyilizu et al*., 2014; *Swallow et al*., 1991; *Shaghude et al*., 2002]. The region is included in several basin-scale [*Matano et al*., 2008; *Hermes and Reason*, 2008; *Mishra et al*., 2007; *Anderson et al*., 1991] and global models [*Sasaki et al*., 2006 (OFES); *Chassignet et al*., 2007 (HYCOM)], but their spatial resolution (~10–30 km) is too coarse to provide insight at the regional scale, and some important small-scale topographic features, like the Zanzibar Archipelago, are inadequately represented. Nearshore and shelf environmental issues, such as the threats imposed by pollution, overexploitation and habitat degradation and their potential impacts on water quality, health, ecotourism, and sustainable recruitment of coral reef dependent species, require higher resolution physical models, capable of resolving small-scale transport processes. Near-field circulation profoundly influences dispersal and recruitment of coral reef organisms and the transport of pollutants. For example, in

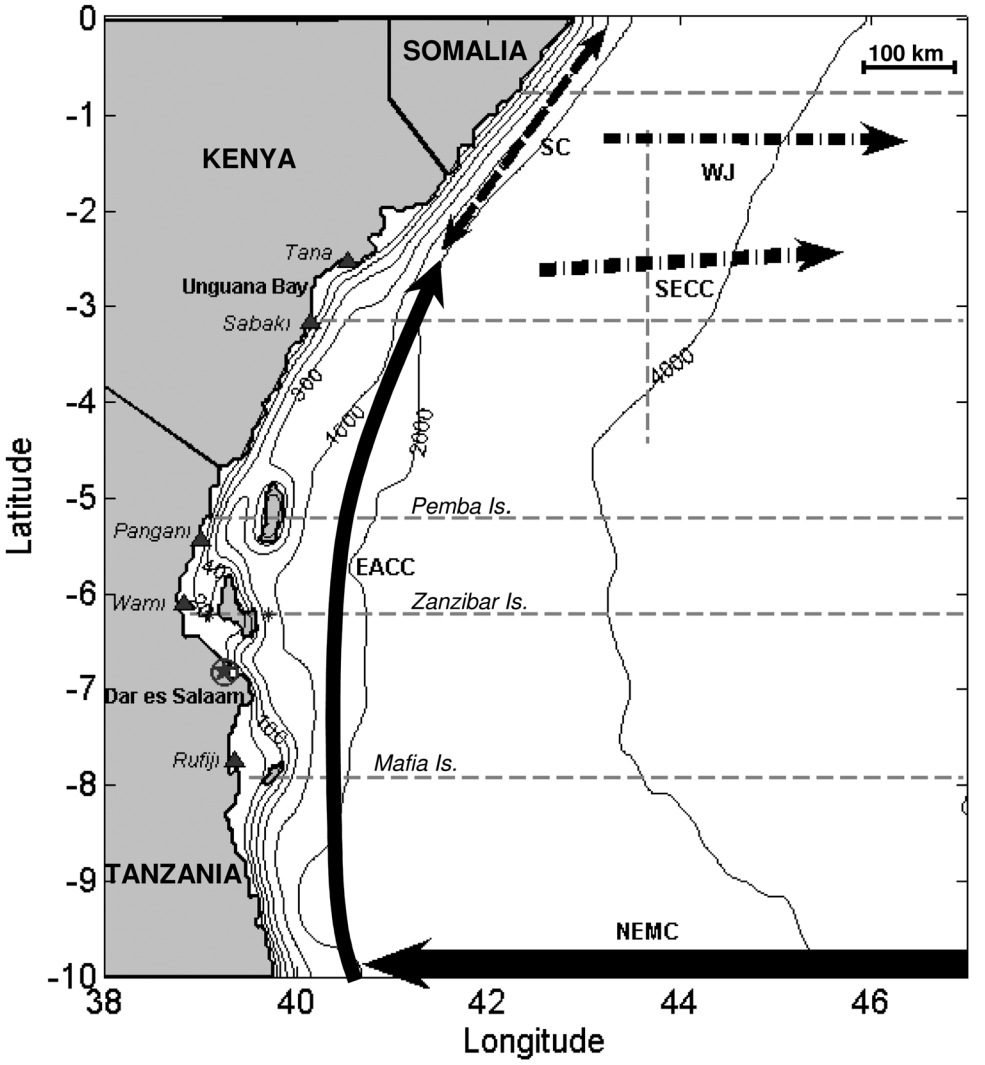

Figure 1. Model domain with schematic arrows showing the main surface currents, solid lines for year-round currents and dashed lines for seasonal currents (see text for details). Triangles mark river mouths. The model coastline and bathymetry are shown, along with locations named in the text. Starting at 5°S, the islands from north to south are Pemba, Zanzibar, and Mafia. Gray dash lines and asterisk mark locations examined for model validation. Bathymetric contours are 20, 40, 100, 300, 1000, 2000, and 4000 m.

studies on coral reefs elsewhere, the important spatial scales for dispersal and recruitment of reef species varied from <5 km for coral larvae [*Sammarco and Andrews*, 1988] to 10–100 km for a variety of coral reef fish species [*Cowen et al*., 2006; *Schultz and Cowen*, 1994]. Prior models [i.e., *Manyilizu et al*., 2014; *Hermes and Reason*, 2008; *Pandey and Rai*, 2008; *Mishra et al*., 2007; *Xie et al*., 2002; *Lee and Marotzke*, 1998; *Anderson et al*., 1991] that include the western Indian Ocean have not provided the resolution needed to address these environmental threats and enable assessment of their impacts.

The Tanzanian continental shelf is very narrow, with the 200 m isobath approximately 12 km offshore, except in the Mafia and Zanzibar Channels, where the shelf width extends ~60 km offshore (Figure 1). Several islands in Tanzanian waters modify the coastal circulation and are of particular concern due to their rich coral reef ecosystems. The Zanzibar Archipelago, ~50 km offshore of the Tanzania mainland, is composed of several islets and two main islands: Unguja (also known as Zanzibar Island), and Pemba. Mafia Island is found farther south. Narrow channels (<60 km width) separate the islands from mainland Tanzania; the Mafia and Zanzibar Channels are shallow (<40 m depth), while the Pemba Channel is much deeper (~500 m maximum depth). The continental shelf north of Tanzania, off Kenya, is also narrow and protected by fringing coral reefs that stretch along the coast, except at the river mouths, where the continental shelf is wider (up to 15 km at the Tana River delta) [*Odido and Mazzilli*, 2009].

The monsoons are the dominant influence on the climate of the region generating a strong seasonality. The coastal circulation off Kenya and Tanzania is mainly influenced by (Figure 1) (1) the northward flowing East African Coastal Current (EACC), fed by (2) the regionally westward flowing North East Madagascar Current (NEMC), (3) the seasonally reversing Somali Current (SC), and (4) local winds. The NE monsoon (November–February) is characterized by weaker winds ($\sim$6 m s^{-1}) from the NE, negative wind stress curl and upwelling along the coast. Farther offshore, wind stress curl is positive [*Collins et al*., 2012] and air temperatures are higher (22–34°C). During this period, the SC flows southward across the equator to meet the northward flowing EACC in a confluence zone between 2° and 4°S, supplying water for the eastward flowing surface South Equatorial Countercurrent (SECC). The SE monsoon (April–September) brings lower air temperatures (19–29°C) and stronger winds (up to 10 m s^{-1}) from the SE, positive wind stress curl, and downwelling along the coast, with negative wind stress curl farther offshore [*Collins et al*., 2012]. During this period, the EACC and the reversing SC create a continuous northward current adjacent to the Tanzanian and Kenyan coasts [*Fieux*, 2001], while the SECC becomes a subsurface current, masked by overlying westward Ekman currents [*Schott et al*., 2009]. The intermonsoon periods, March–April and October–November, are characterized by winds with lower speed and more variable direction [*Schott et al*., 2009; *Odido and Mazzilli*, 2009; *Schott and McCreary*, 2001]. At these times, the *Wyrtki* Jets appear. These are strong eastward surface jets trapped within 2°–3° north and south of the equator that uplift the thermocline in the western Indian Ocean (Figure 1) [*Fieux and Reverdin*, 2001; *Wyrtki*, 1973]. There are two rainy seasons: the long rains during March–May and the short rains during November and December, with the maximum precipitation (approximately 20 cm $month^{-1}$) occurring during April and May [*Odido and Mazzilli*, 2009].

In addition to local atmospheric forcing and remote forcing created by the large-scale circulation, tidal currents are known to have an important effect on the inshore circulation of these regions [*Shaghude et al*., 2002; *van Katwijk et al*., 1993; *Mayorga-Adame*, 2007]. Freshwater inputs from rivers during the rainy seasons are also important in structuring shelf currents and hydrography [*van Katwijk et al*., 1993], while diurnal variability of the local winds affects the nearshore surface currents.

Due to the challenges posed for field work in the region, our approach is to develop a high-resolution model to characterize the circulation of the Kenyan-Tanzanian region at temporal and spatial scales relevant to local environmental issues. We developed a high-resolution (4 km horizontal grid spacing) Regional Ocean Model System (ROMS) [*Haidvogel et al*., 2008] application and validate it with satellite observations and available in situ measurements. This Kenyan-Tanzanian Coastal Model (KTCM) is used to investigate the influence of local atmospheric forcing, remote forcing through the model open boundaries and tidal forcing on the circulation and hydrography of the Kenyan-Tanzanian coast off East Africa. Forcing by freshwater input from rivers and the diurnal variability in local winds are not included in the present model.

The methods used are reviewed in section 2, including descriptions of the model (section 2.1), the lateral boundary conditions (section 2.2), the surface forcing (section 2.3), initial conditions (section 2.4), and the methods used to validate the model results (section 2.5). Results are presented in section 3, where we first compare model results to available satellite and in situ observations (section 3.1). The seasonality of the circulation and hydrography of the full model domain is presented in section 3.2, followed by a detailed examination of the circulation of the coastal region within 60 km of land (section 3.3). It is in the coastal region that the increased resolution of KTCM provides information relevant to the coastal environment of Kenya and Tanzania that is not available from previous studies [i.e., *Hermes and Reason*, 2008; *Shaghude et al*., 2002; *Swallow et al*., 1991]. In section 4, we discuss the significance of our results, and summarize our findings in section 5.

2. Methods

2.1. Model Overview

We use ROMS, a three-dimensional, hydrostatic, terrain-following, primitive equation model [*Haidvogel et al*., 2008] to simulate the circulation in the coastal ocean off Kenya and Tanzania. The model domain is a rectangular grid extending from 38° to 47°E and from the equator to 10°S (Figure 1). It has a uniform horizontal resolution of 4 km and 31 vertical sigma levels with increased resolution toward the surface and the bottom. Inshore of the 500 m isobath, vertical resolution is finer than 20 m at intermediate depths; offshore, where depths exceed 3500 m, intermediate depths have approximately 300 m vertical resolution.

Bathymetry for the region was created by fusing data from multiple sources: (1) ETOPO-02, (2) digitized nautical charts of the region, and (3) sounder depth measurements collected by researchers of the Institute of Marine Sciences (IMS) of the University of Dar Es Salaam. This improved the bathymetry of the Zanzibar Channel, which is not accurately represented in the ETOPO-02 database. Near the eastern open boundary of the model domain (~920 km offshore), Aldabra and other smaller islands of the Comoros Archipelago were flattened to 4000 m depth to avoid numerical noise at the open boundary. Bathymetry was smoothed to meet a "slope factor" $r < 0.2$, in order to reduce pressure gradient errors in terrain-following coordinates [*Beckmann and Haidvogel*, 1993]. The model coastline was manually modified to retain as many features as the 4 km horizontal resolution allowed. Only the islands of Zanzibar, Pemba, and Mafia were included as dry cells in the land mask. The northern, southern, and eastern edges of the model domain are open boundaries. A third-order, upwind-biased scheme was used for horizontal advection of momentum and tracers. Since clear water characterizes the region, Jerlov water type 1 was used [*Jerlov*, 1976]. A fourth-order, centered scheme was used for vertical advection of momentum and tracers. The generic length scale closure scheme [*Warner et al*., 2005; *Umlauf and Burchard*, 2003] with *k-kl* (Mellor-Yamada level 2.5) parameters [*Mellor and Yamada*, 1982] is used for vertical mixing. The Chapman open boundary condition was used for the free surface and the method of Flather for the depth-averaged velocities normal to the open boundaries [*Marchesiello et al*., 2001]. Radiation and nudging schemes were applied to the three-dimensional velocities and tracers at the boundaries. The nudging time scale was 20 days for outflow and 2 days for inflow. Since numerical noise was not generated at the open boundaries, no sponge layer was used.

2.2. Boundary Conditions

The boundary conditions provide tidal and remote forcing to the model. Tidal forcing was obtained from the TPXO7 [*Egbert et al*., 1994; *Egbert and Erofeeva*, 2002] Indian Ocean 2011 tidal solution atlas, with a resolution of 1/12° in the study region. The tidal ellipse information and sea surface elevation harmonics were processed by ROMS to add the SSH and velocities contributed by tides to the boundary forcing. The nine main tidal components: M4, K2, S2, M2, N2, K1, P1, O1, and Q1 were included as forcing to KTCM.

Remote forcing at the open boundaries is driven by the gyre-scale wind stress curl and the resulting oceanic pressure fields that set up the large-scale current system. Monthly open boundary conditions (temperature, salinity, sea surface height, and horizontal and vertical velocities) were extracted from the global Ocean General Circulation Model (OGCM) for the Earth Simulator (OFES) [*Sasaki et al*., 2006]. The OFES simulation has a horizontal grid spacing of 1/10° (approximately 10 km in this region) and 54 fixed depth vertical levels. It was forced by daily mean QuickSCAT wind stress and atmospheric daily mean heat and salinity fluxes from the NCEP/NCAR reanalysis [*Kalnay et al*., 1996]. Remote forcing is summarized by examining the climatological volume transport across the open boundaries of the domain in the upper 500 m obtained from the "parent model" OFES (Figure 2). The strongly seasonal flow and the abrupt transitions between monsoons broadly agree with observations [*Schott et al*., 2009; *Schott and McCreary*, 2001]. During the NE monsoon, the primary transport balance is between inflow from the south and outflow to the east. During the SE monsoon, the inflow from the south is joined by greater inflow from the east, from the seasonally broader NEMC, resulting in even greater outflow to the north (Figure 2). The transport across the boundaries shows that the remote forcing imposes two main balances on the model: (1) during May–November (red arrows in Figure 2, inset), inflow from the south and east is balanced by outflow through the northern boundary and (2) during January–March (blue arrows), the inflow from the south is balanced by outflow through the eastern boundary since the outflow through the northern boundary is blocked by the influence of the southward flowing SC (Figure 2, inset).

2.3. Surface Forcing

Local atmospheric forcing consists of wind stress, heat, and precipitation/evaporation fluxes that operate on the surface of the model domain. Surface forcing for KTCM was provided by daily mean atmospheric variables (air temperature and pressure, precipitation rate, relative humidity, solar radiation, downward longwave radiation, and the two components of the wind velocity) from the NCEP/NCAR reanalysis with a resolution of 1.8° [*Kalnay et al*., 1996]. Atmospheric variables were bilinearly interpolated to the model grid. Wind stress, heat, and fresh water fluxes were calculated by the ROMS atmospheric bulk formulation. Neither OFES nor KTCM assimilate observations.

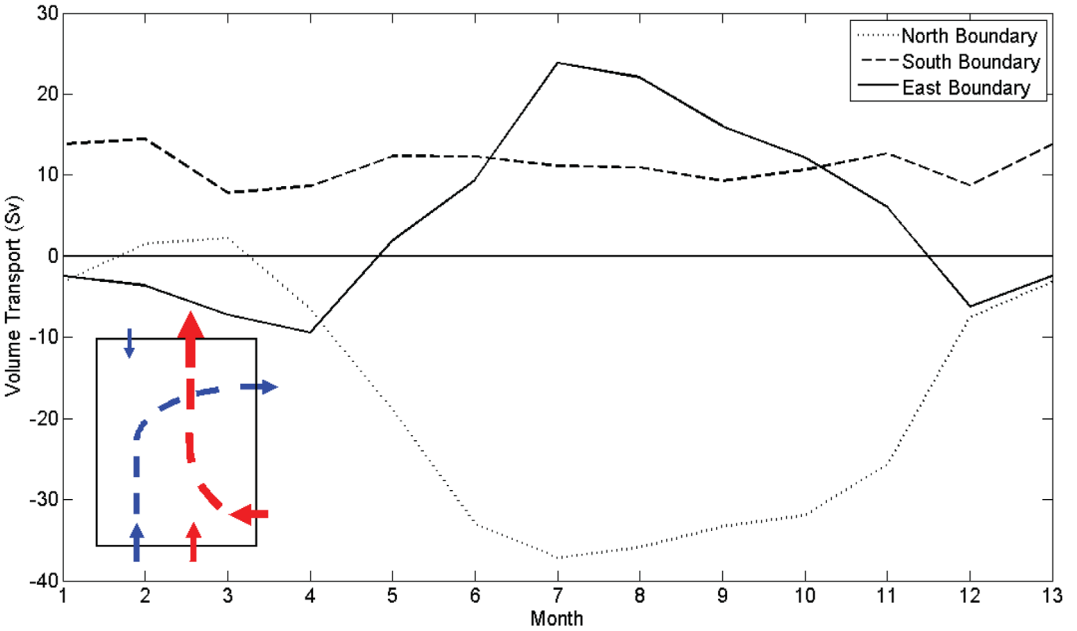

Figure 2. Volume transport in the upper 500 m in Sverdrup's (Sv = 10^6 m^3 s^{-1}) across the three open boundaries of the model domain. Positive (negative) values represent transport into (out of) the domain. The inset represents the main flow balances in the model domain for January–March in blue and for May–November in red.

Of the local forcing variables, wind forcing has the strongest influence on the circulation of the modeled region. *Collins et al*. [2012] compared the NCEP wind product to QuickSCAT winds and concluded that despite its coarser resolution the NCEP reanalysis accurately represents the large-scale wind patterns over the western tropical Indian Ocean. They describe important differences in the Somali Jet region north of our domain and around oceanic islands. QuickSCAT winds could make an important difference if the scatterometer was able to measure winds around the islands in our domain. However, there are no vectors inshore of these islands in the QuickSCAT wind product. Therefore, we used NCEP winds for consistency with the other atmospheric forcing variables. The long term climatology of the wind forcing from 2000 to 2007 shows SE winds from April to November and NE winds in January and February (Figure 3). The transition between SE and NE monsoons winds (and vice versa) happens very quickly. Intermonsoon conditions in the atmosphere, with weak onshore winds, are observed only in March and December.

2.4. Initialization

Transient model responses associated with initialization were reduced by doing a 22 month ROMS spin-up from initial fields interpolated from the January 2000 OFES fields and climatological forcing (an average of 2000–2007 monthly boundary conditions from OFES and averaged daily surface forcing from the NCEP/NCAR reanalysis). Conditions at the end of the spin-up run were used as the initial conditions for an 8.25

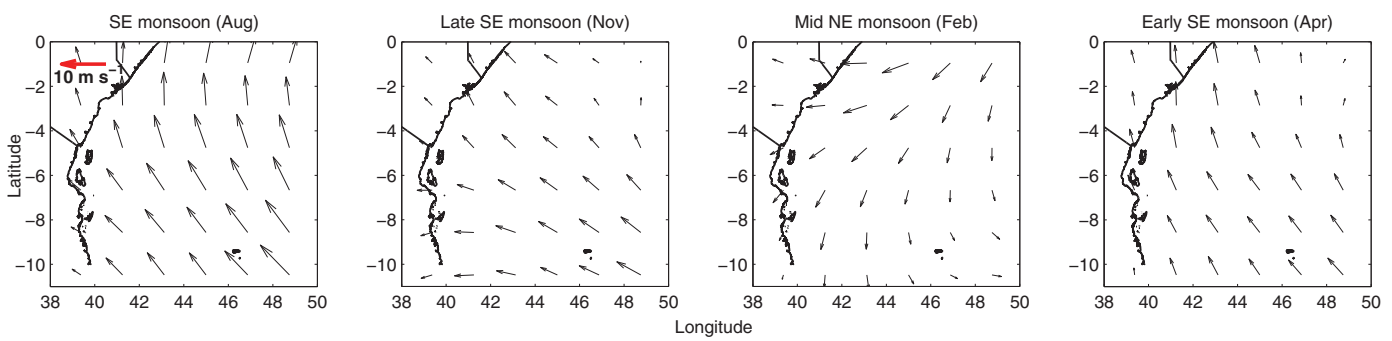

Figure 3. Climatological monthly mean of the NCEP-NCAR wind speed vectors used to force the model. Months shown are representative of the seasonality of the region: early (April), mid (August) and late (November) SE monsoon; NE monsoon (February).

year simulation (from October 1999 to December 2007). The first 3 months of the simulation were discarded to eliminate transient adjustments to the stronger and more realistic daily forcing. Results of the 8 year (2000–2007) simulation were averaged to form a monthly climatology. This yields a realistic representation of nonlinear responses within the ocean to strong and rapidly changing surface forcing. The results describe the averaged response to energetic forcing, rather than the response to averaged (weaker and smoother) forcing obtained when forcing with climatological fields. We use this monthly climatology to examine the seasonal circulation off Kenya and Tanzania.

2.5. Model Validation

Year specific model results are compared with Pathfinder v5 satellite SST [http://www.nodc.noaa.gov/sog/pathfinder4km/], altimeter sea level anomaly (SLA) fields from AVISO [Archiving, Validation, and Interpretation of Satellite Oceanographic data, http://www.aviso.altimetry.fr/] and World Ocean Database 2009 (WOD09) temperature profiles [https://www.nodc.noaa.gov/OC5/WOD09/pr_wod09.html]. Since there were too few salinity profiles in the WOD09 that overlapped our time period and they contained spurious data, we compared model salinity to a published salinity section [*Swallow et al*., 1991] that we consider representative of the subsurface salinity features, despite not corresponding to the modeled period. To make direct model-data comparisons, the model results were interpolated to the locations of the satellite gridded products using bilinear interpolation. The SST interpolation did not imply a change in resolution since both model and Pathfinder v5 SST have a grid spacing of 4 km. The AVISO SLA product has a grid spacing of $1/4^{\circ}$ ($\sim$30 km), therefore the interpolation was to the coarser AVISO grid. To provide comparable model SSH and altimeter SLA data, the long-term mean SSH of the model was added to AVISO SLA to create absolute dynamic topography fields, which we simply refer to as SSH. Temperatures at standard hydrographic depths were extracted from the daily averaged model at the positions and dates of the observed WOD09 profiles within the modeled period (2000–2007).

To quantitatively assess the skill of the model to reproduce satellite SST and SSH, we calculated metrics that summarize the variability, differences between modeled and observed values (after removing the mean of each field), and similarity of variability patterns, i.e., normalized standard deviations ($n\sigma_m$), normalized root-mean-squared errors (*nRMSE*) and correlation coefficients (*r*), respectively [*Taylor*, 2001]. Agreement between model and satellite SSH was examined using an Empirical Orthogonal Functions (EOF) analysis on the detrended model and altimeter SSH.

Comparisons of the model and satellite fields should note the sources of error in the satellite data, as well as in the model fields. The AVHRR SST fields, in particular, are subject to several types of error. The infrared (IR) signal from the sea surface originates in the top (1 mm or less) skin of the ocean, which can be either colder or warmer than the ocean in the upper several centimeters or meters. This can combine with warming of the top several meters of the water column during periods of calm winds, when a warm upper layer of the ocean develops that masks temperature signals associated with more dynamic processes such as upwelling and advection of SST gradients. In the tropics, there are also problems in the atmospheric correction due to the high humidity in the atmosphere. Atmospheric correction algorithms account for absorption by water vapor but may be in error as humidity increases. Finally, the cloud mask is a notorious problem. The edges of clouds and small, subpixel sized clouds are especially difficult to detect, although algorithms attempt to do this. These problems are described in texts such as *Martin* [2014] and in chapters of *Barale et al*. [2010]. Problems with the altimeter are greatest in the regions next to land, due to radar reflections from the land as described by *Gommenginger et al*. [2011]. These potential problems with the satellite data should be kept in mind when comparing to the model fields. Below we note instances where these artifacts may affect the satellite data.

3. Results

3.1. Comparisons to Observations

We start with an evaluation of model performance in its full domain, before presenting the model representation of seasonal changes in surface circulation, temperature, and salinity. The goal is to represent the larger-scale circulation and water properties as well or better than previous regional models. We then focus on the seasonal cycles in the coastal region surrounding the islands off Tanzania, where the model provides details not available from earlier, coarser-scale models.

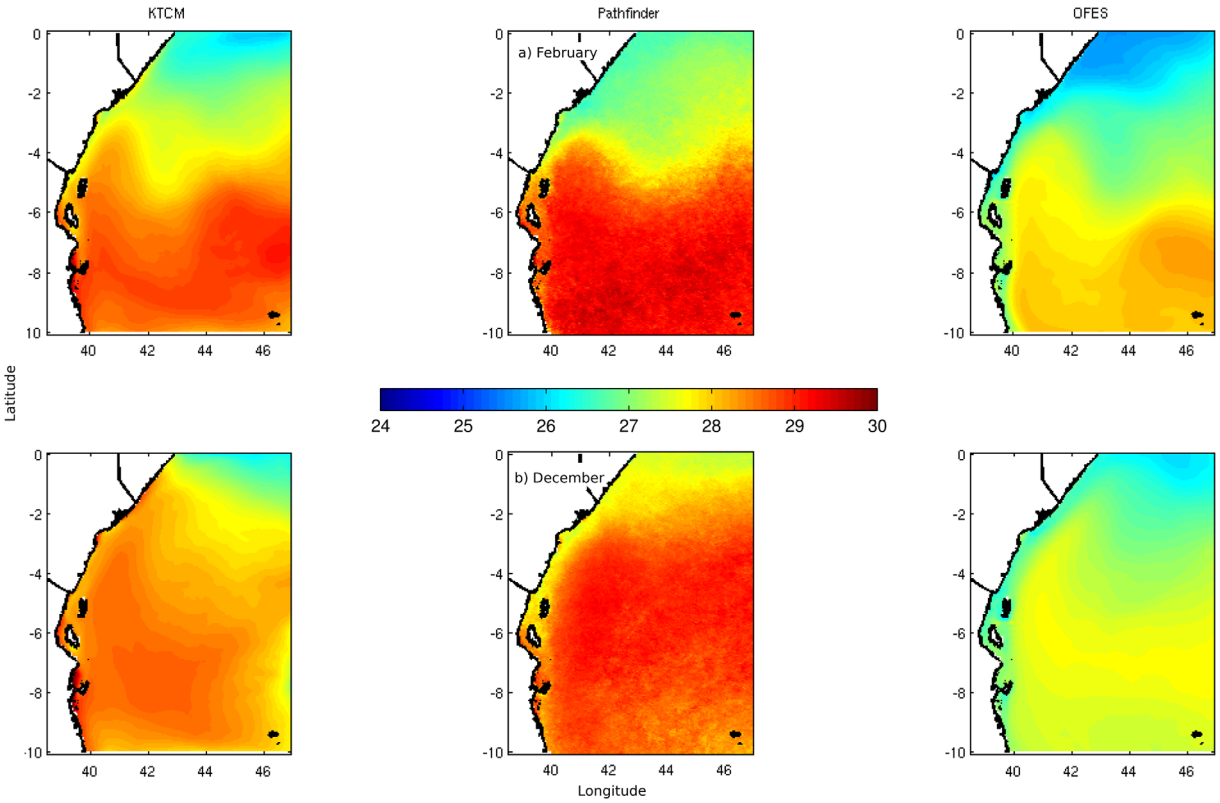

Figure 4. Sea surface temperature (°C) from KTCM, Pathfinder and OFES for two different months: (a) February (NE monsoon) and (b) December (transition).

SST climatological means from 2000 to 2007 are shown in Figure 4 for months in which the correlations between the model and satellite SST fields are high (February, $r = 0.78$) and low (December, $r = 0.34$). The KTCM's SST variability is more similar than OFES to the satellite SST in all months except March, when variability is slightly overestimated by our model. Although OFES SST fields produce a lower *nRMSE* when compared to Pathfinder SST than KTCM, the OFES SST has a cold bias relative to the satellite observations, with differences of up to 2.8°C (Figure 4). The smallest OFES SST biases occur during June–September (<1.5°C) but bias relative to Pathfinder are never less than ±0.5°C. In contrast, KTCM SST fields are within ±0.5°C of the satellite observations in most of the domain during every month.

A relatively cool SST band in the coastal shelf region extends from the northern boundary to 4.5°S in February and to 6°S in December in the Pathfinder SST. This band stretches unrealistically along the entire coast in the OFES model. In KTCM, the extension of this feature is very similar to that of Pathfinder in both months. In December, however, the across-shore temperature gradient in KTCM is weaker than in the satellite SST. KTCM SST is slightly cooler at the open boundaries, especially in the north, likely due to the influence of the OFES boundary conditions. This has only a minor impact on the interior of the domain where KTCM reproduces fairly well the satellite SSTs (Figure 4).

Hövmuller diagrams in Figures 5c and 5d provide comparisons between monthly satellite and KTCM SST time series for the full east-west transect across the model domain at 6.2°S for the 8 years modeled. Good agreement is observed between model and satellite annual cool and warm periods. KTCM slightly underestimates the magnitude and duration of warm periods in the deep basin east of the island. This transect is representative of the other four east-west transects examined, as well as the north-south transect at 43.3°E in the northern half of the domain, where variability is maximum (gray dashed lines in Figure 1). Point to point comparisons between monthly SST time series at several locations along these transects show similar results for all locations, indicating good agreement between modeled and observed SST temporal variations ($r > 0.85$, $p < 0.01$ for all locations). An example is shown in Figures 5a and 5b for two locations (marked with * in Figure 1 at 6.2°S), inshore and offshore of Zanzibar Island. Although the KTCM shows a tendency

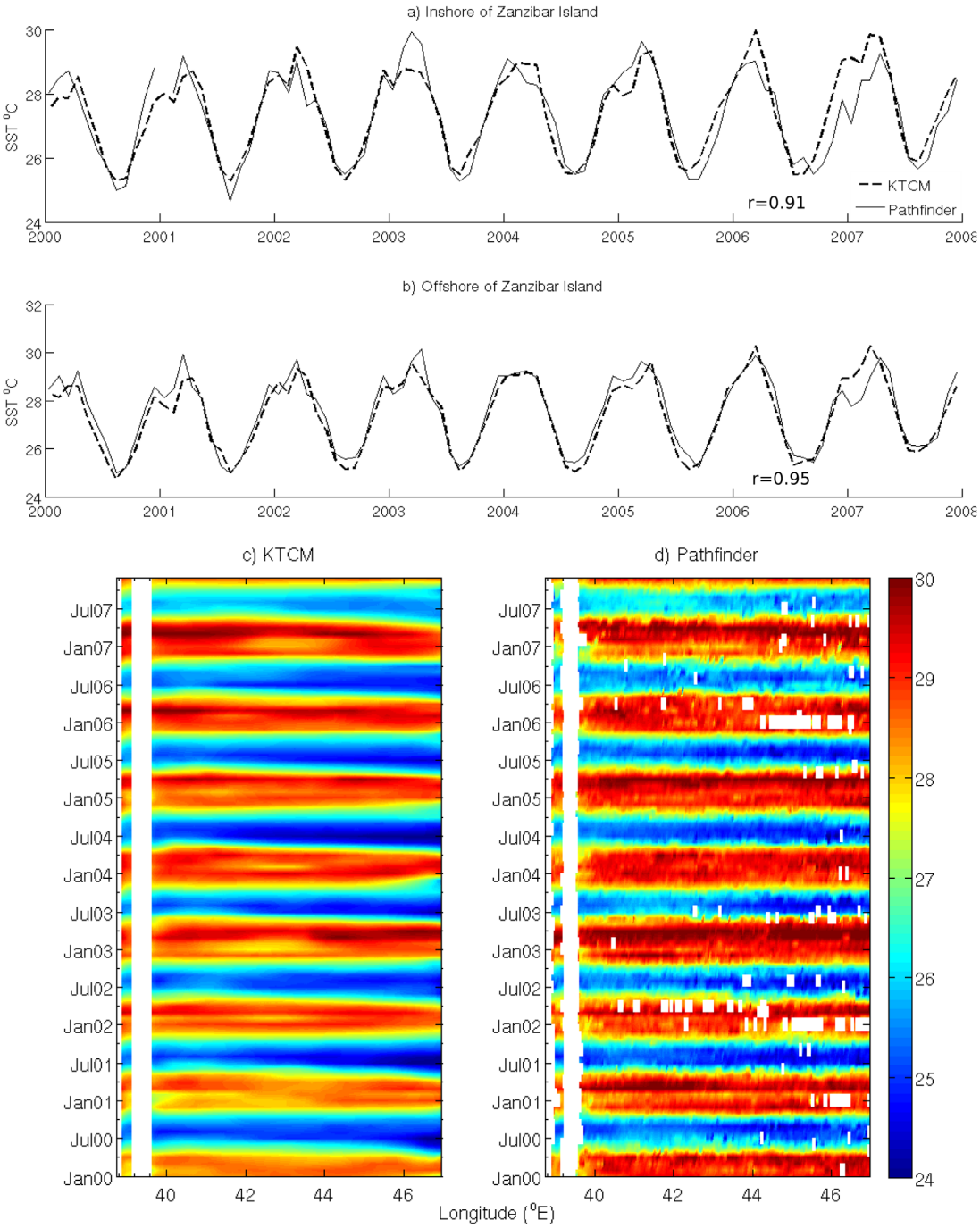

Figure 5. SST time series comparisons between KTCM and Pathfinder satellite observations: (a) inshore and (b) offshore of Zanzibar Island (6.2°S). Hövmuller diagrams of SST along the transect at 6.2°S from (c) KTCM and (d) Pathfinder satellite.

to slightly over or underestimate the magnitude of the seasonal extremes, it agrees with the Pathfinder data in reproducing two relative maxima in SST in most years—a minor peak in December–January and a major peak in March–April (evident also in the Hövmuller diagrams). Years 2004 and 2006 are the exceptions for both KTCM and satellite SST, providing some confidence in the model's ability to capture interannual variability.

Looking next at sea surface heights, climatological monthly means of the "parent model" OFES, KTCM, and altimeter SSH are shown in Figure 6 for June (early SE monsoon) when the model hindcasting skill is high

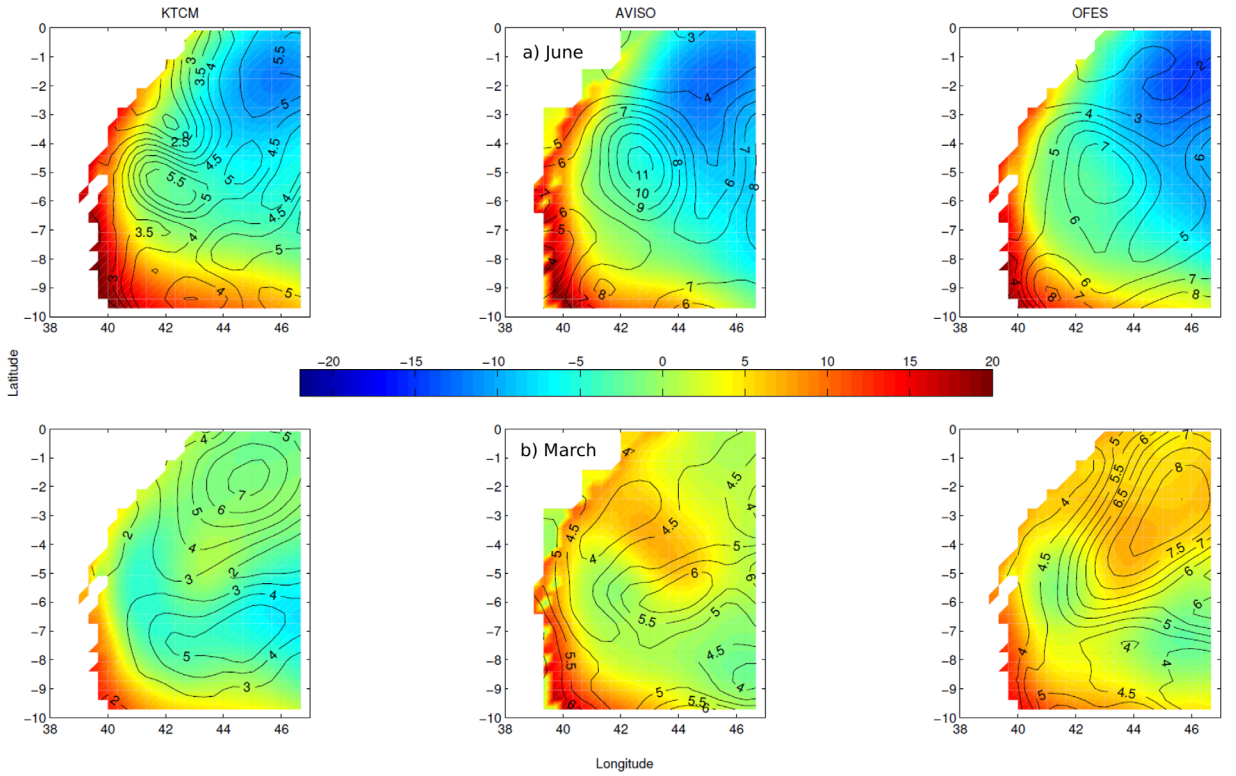

Figure 6. Sea surface height (colors) in centimeters from KTCM, AVISO, and OFES for two different months: (a) June (early SE monsoon) and (b) March (late-NE monsoon), with overlaid contours of interannual variability (standard deviations) among the 8 years modeled.

(r = 0.85) and March (late NE monsoon) when it is low (r = 0.32). Correlation coefficients and *nRMSE* values comparing OFES and KTCM SSH to AVISO were very similar. However, the SSH variability from KTCM is more similar than OFES to the AVISO SSH in all months. The climatological mean SSH from KTCM and OFES compare well with AVISO in June (when nearshore-offshore gradients in SSH are strong and smaller-scale spatial variability is low); however, both models show less interannual variability than AVISO. For March (when gradients in SSH are weaker and local spatial variability is more prominent), the comparison of climatologies is less satisfactory. The mean SSH patterns of both models are poorly correlated with the mean satellite observations in the northern half of the domain (Figure 6b). The positive SSH feature that extends from the northern coast to the center of the domain in AVISO is hardly noticeably in KTCM. OFES has this positive SSH feature but it occupies the entire northeastern corner of the domain. During this month altimeter SSH shows less interannual variability and both models are within a similar range, due to the direct influence of OFES boundary conditions on KTCM's SSH patterns. In general, KTCM shows less skill in simulating SSH during the NE monsoon (represented by March in Figure 6), a season characterized by more dynamic mesoscale features, especially meanders and eddies, generated by the confluence of the SC and the EACC and westward propagating eddies generated near the equator. Even though the model fields include a comparable number of mesoscale features, with characteristics similar to those of the satellite observations, it is difficult to simulate these highly variable mesoscale features at the right time and place in a model that does not include data assimilation. KTCM shows higher skill in representing the NE monsoon SSH (represented by June in Figure 6), characterized by strong continuous northward flow and more static conditions.

The Hövmuller diagrams for the east-west transect at 8°S (Figures 7a and 7b) show a slightly larger amplitude seasonal cycle for the model than the altimeter. The model represents well the offshore extent of the EACC and its interannual variability, although there are examples of both underestimates and overestimates of the intensity of that variability. Several specific events with positive SSH extending far offshore are not reproduced by the model (e.g., in the first half of 2005 and again in 2007). At other times, the model produces extended offshore features not found in the altimeter data. These discrepancies are typical of model simulations that produce features similar to those found in observations but at different places and/or

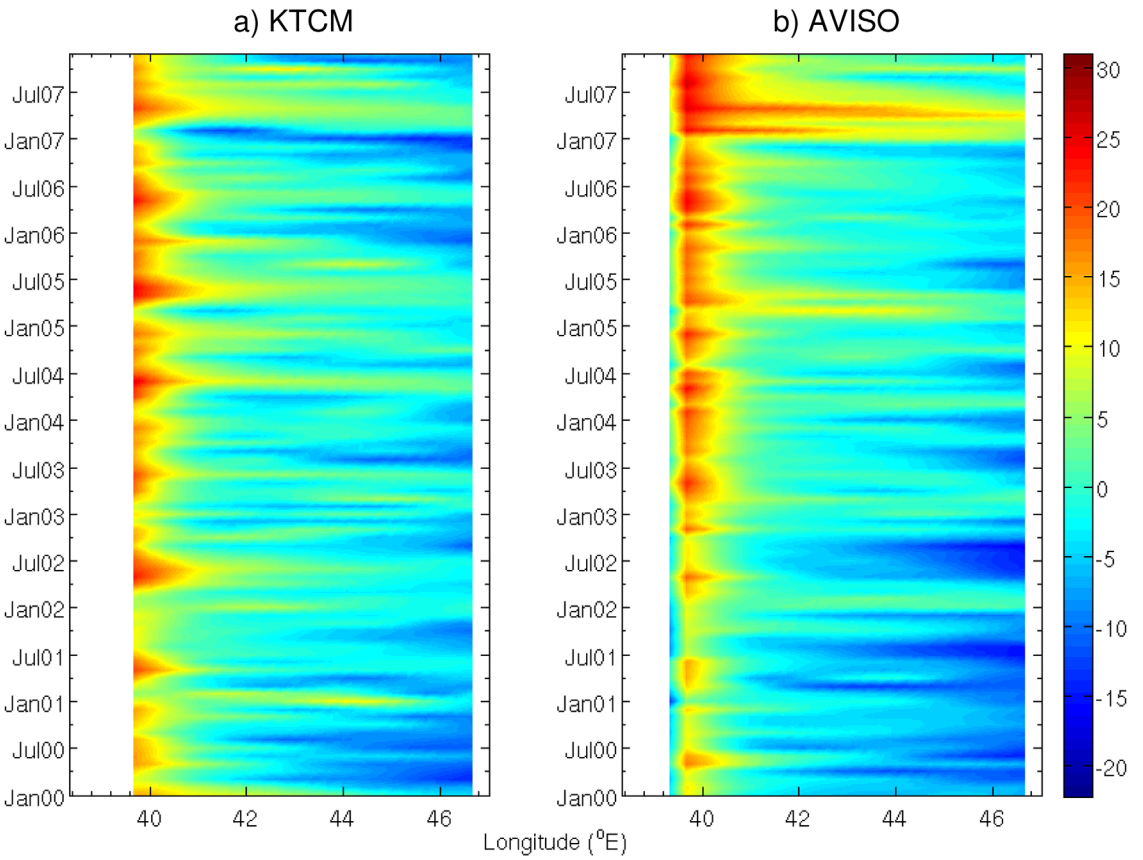

Figure 7. Hövmuller diagrams of SSH along a transect across the modeled region at 8°S from (a) KTCM and (b) AVISO.

times. Such discrepancies are reduced in models that include data assimilation, which is not incorporated into our model. At the beginning of the time series, AVISO SSH shows stronger negative values than KTCM in the open ocean (eastern side of the domain), a pattern that reverses by the end of the time series. This may results from the decadal trend in global sea level, which amounts to a rise of approximately 2 cm over the 8 year period. The AVISO data include a band of low SSH at the far western boundary of the transect, next to the land. This is most likely an indication of land contamination of the altimeter's radar signal [*Gommenginger et al*., 2011]. Comparisons shown in Figure 7 are representative of other locations examined (gray dashed lines in Figure 1).

The spatial patterns of the first EOF of SSH from AVISO and KTCM compare relatively well (Figures 8a and 8b). Their time series capture many of the same events ($r = 0.43$, $p < 0.01$), although the mean of the model's time series is greater than that of AVISO. The first mode in both the model and satellite SSH explains approximately half of the overall variance. The spatial similarity of the first modes indicates that the KTCM captures the main SSH patterns seen by the satellite. KTCM better represents SSH variability nearshore than offshore because in the nearshore region SSH variability is dominated by tidal fluctuations, which are well represented in the model. Offshore SSH results from the interaction of several processes (e.g., tides, remote forcing at the open boundaries, and local wind stress) and is therefore harder to reproduce by a nonassimilating ocean circulation model like KTCM.

In order to assess the model representation of subsurface conditions, we plot KTCM temperatures versus WOD09 in situ subsurface temperature observations from the same time and location (Figure 9). This shows that the model does a reasonable job at representing observed subsurface temperatures (points cluster well along the 1:1 line). The model simulates vertical structure slightly better in coastal ocean regions shallower than 2000 m (Figures 9a and 9c). In the deeper regions, it does a better job in the southern half of the domain (Figure 9d) than in the north (Figure 9b). The greatest discrepancies between model and observed temperatures are found in the main thermocline (75–250 m, gray circles). The low vertical resolution of our

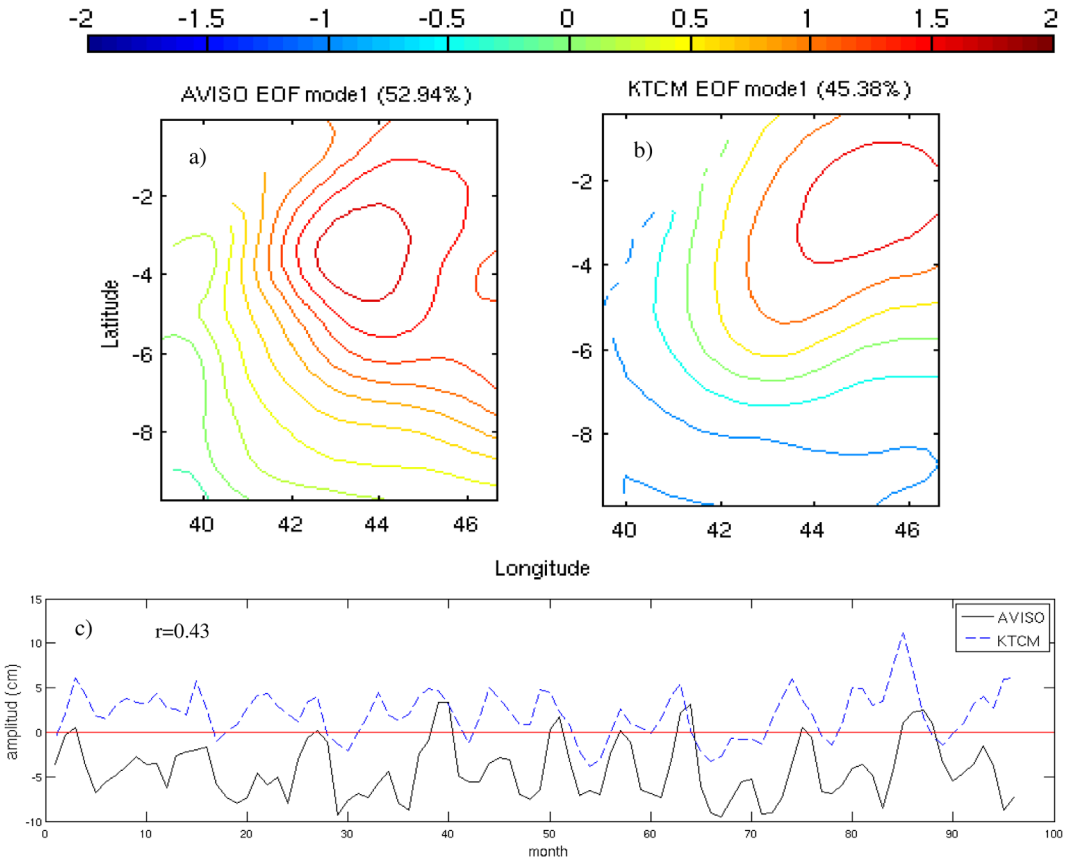

Figure 8. Spatial pattern of the first EOF mode of SSH (cm) for (a) AVISO and (b) KTCM. (c) The amplitude and temporal variability of the patterns is shown for this mode, including the correlation coefficient (r) between the two time series. The color bar at the top applies to Figures 8a and 8b. The solid black line in Figure 8c is the AVISO time series; the dashed blue line is the KTCM time series.

model at those depths (25–70 m offshore of the 2000 m isobath) may be responsible for the mismatch. The primary processes affecting temperature in the thermocline include vertical mixing of heat downward and internal displacements of isotherms caused by internal waves and tides, which we do not expect to be coherent in time between model and observations.

As a qualitative check on the model representation of subsurface salinity, given the lack of more representative observations, the modeled salinity climatology for April at 5°S was compared to a salinity section based on observations from April 1985 [*Swallow et al.*, 1991] (Figure 10). Several salinity features of the observed section are represented in the modeled April climatology—low salinity surface water inshore, a strong halocline between 50 and 200 m depth, and an offshore core of high salinity near 200 m depth that extends eastward toward the surface. Interannual variability among the eight model years is mainly observed in the offshore extent of the low salinity surface water and the tilting of the deep 35 and 34.9 PSU haloclines (not shown).

Only indirect comparisons of volume transports in our domain are possible since observed transports are reported for specific sections and times, while we have the climatological monthly mean transport across the model boundaries (Figure 2). Flow through the southern boundary of the domain is inward throughout the year, but fluctuates between 8 and 15 Sv. The main contribution to this transport is the northward flowing EACC. *Swallow et al.* [1991] report an observed EACC transport of 10 Sv in the upper 100 m for April, 1985, at 5°S. Modeled transport through the northern boundary varies from approximately 2 Sv southward (inward) during February–March to 30–40 Sv northward (outward) during June–October (Figure 2). *Schott et al.* [1990] report a similar seasonality with close to 0 Sv mean transport across the equator in the upper 500 m during the NE monsoon (December–February), and 21 Sv northward (outward) mean transport for the SE monsoon period (June–September). This variability is related to the reversal of the Somali Current.

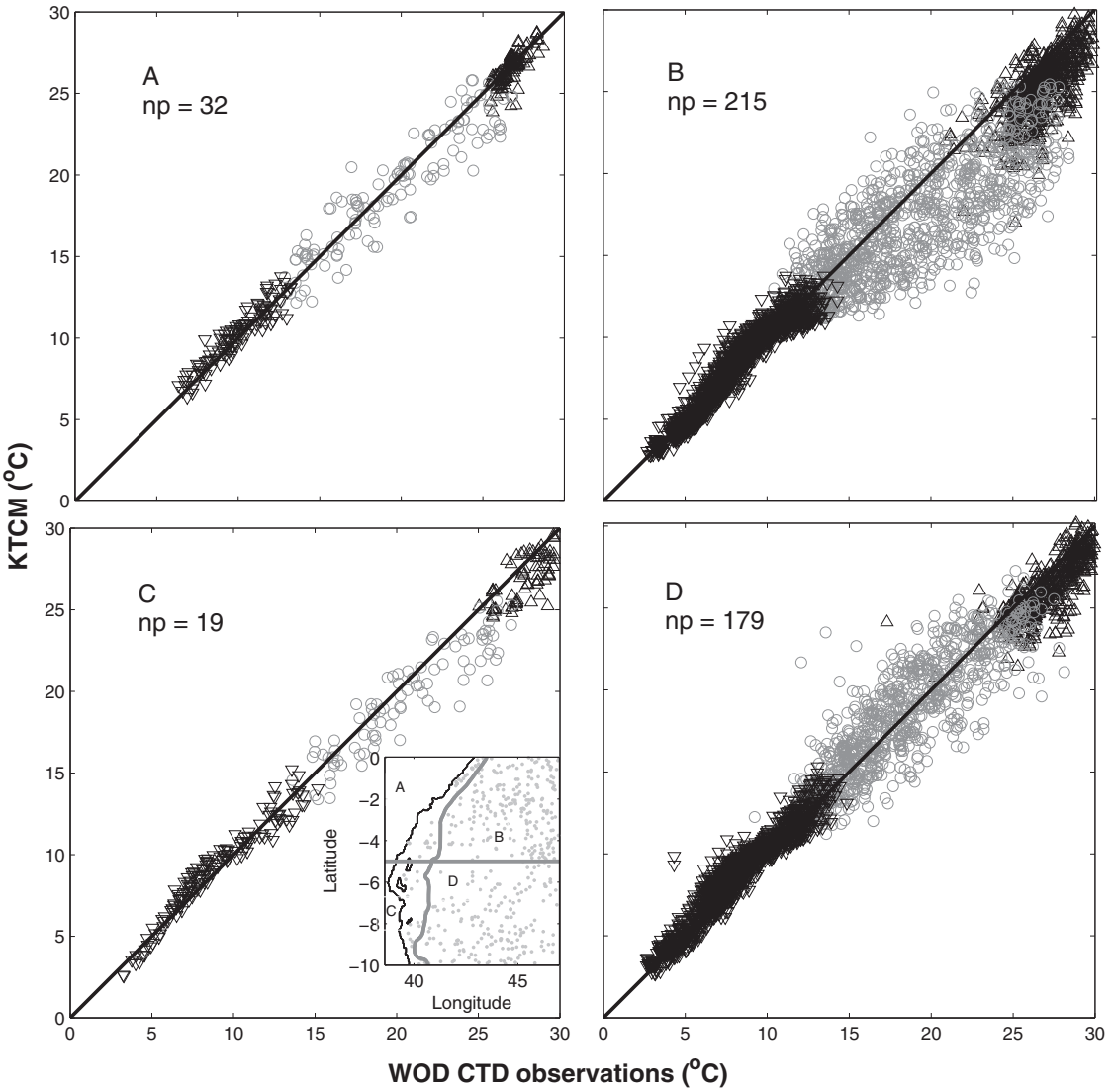

Figure 9. WOD09 observed temperatures at standard depths versus KTCM modeled temperatures. Observed profiles are divided according to the bottom depth in water (A, C) shallower and (B, D) deeper than 2000 m and (A, B) north and (C, D) south of 5°S, as shown in the inset map in Figure 9c. Different symbols mark temperatures at three different depth ranges: (△) 0–75 m, (○) 75–250 m, and (▽) deeper than 250 m; np = number of profiles. A diagonal 1:1 line is shown (not a regression line).

The modeled transport through the eastern boundary is the opposite of that through the northern boundary, with an offset due to the relatively constant flow from the south. It is westward (inward) from June to November, peaking in July, and eastward (outward) during the rest of the year with a peak in April. The flow through this boundary is strongly influenced by the complex equatorial dynamics affecting the model domain circulation. During the NE monsoon period (December–February), the offshore jet generated by the convergence of the SC and the EACC forms the surface SECC that flows to the east between 2° and 8°S. The eastward flowing Wyrtki jet is present at 2°–3°S during the intermonsoon periods (March–April and November). Both the Wyrtki jets and the SECC are responsible for the eastward (outward) flow. The transport into the domain through the eastern boundary is due to the intensification of the NEMC, the north part of the bifurcated SEC that flows westward (inward) year round to the south of our domain but reaches its maximum northward extent (~8°S) during July and August [*Fieux*, 2001; *Schott and McCreary*, 2001]. *Swallow et al*. [1991] report an observed SECC transport of 23 Sv eastward (outward) in the upper 300 m for April, 1985, at 5°S. According to *Wyrtki* [1973], the combined transport of the SECC and the eastward equatorial jet in April–May is 13 Sv in the upper thermocline, while during October–November, the eastward equatorial jet transports 14 Sv eastward (outward).

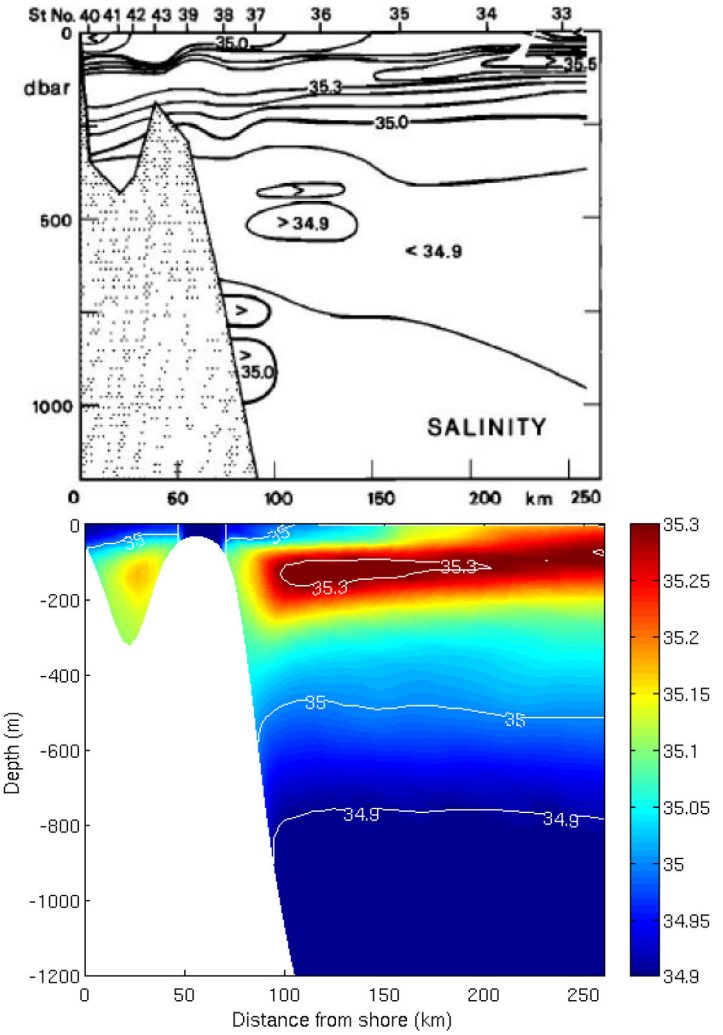

Figure 10. Salinity contours on a vertical section at ~5°S. (top) Based on ship observations made in April 1985 (after *Swallow et al.* [1991]). (bottom) KTCM monthly mean April salinity for the same section.

3.2. Seasonality of Circulation, SST and SSS Patterns

To describe the spatial and seasonal variability of the circulation, SST and SSS, we define the monsoon seasonality using the alongshore surface current patterns rather than the more commonly used wind patterns. Thus, April and November represent intermonsoon periods in the ocean, lagging the wind field by approximately 1 month. The SE monsoon season (May–October) is characterized by continuous northward flow along the entire coast; the NE monsoon season (December–March) has the southward flowing Somali Current intruding into the northern part of the modeled domain. Surface heat and freshwater fluxes strongly influence SST and SSS, respectively. The spatially mean climatological net heat flux shows that the ocean is heating from July to November, while the main cooling period is from March to June. The main component of the net climatological heat flux is the short wave radiation, which is modulated by the latent heat loss. The evaporation-precipitation climatological curve shows two local minima in May and October, and maxima during August–September and January–February. The surface forcing alone would lead to more spatially uniform SST and SSS patterns than observed. This highlights the importance of advection of different water masses on determining surface temperature and salinity patterns in the region. The description that follows is based on the full monthly climatology (see supporting information).

3.2.1. Southeast Monsoon (May–October)

The circulation of the SE monsoon is represented by August in Figures 11 and 12. The EACC flows northward along the entire coast of the model domain (Figures 11a, top row and 12a), reaching its maximum speed (>1 m s^{-1}) and offshore extent in the northern part of the domain in June (i.e., the 80 cm s^{-1} isotach at the surface is >150 km offshore). From May to July, the northward flow occurs in the upper 300 m, but during September and October the 5 cm s^{-1} isotach extends down to >900 m depth. A north-south gradient of the northward alongshore transport is observed during this season, with slower velocities in the southern region of the domain and stronger velocities in the north (Figure 11a, top row). This alongshore flow divergence is compensated by the westward inflow of the northward extended NEMC through the eastern open boundary between 8° and 10°S and even stronger inflow in the northern half of the domain with maximum currents between 2° and 4°S. The combination of this northern inflow and the northward flowing EACC produces a cyclonic feature in Figure 11a (top row) known as the Southern Gyre (SG) [*Schott and McCreary*, 2001, Figure 1a]. SST is uniformly "cold" in August (~24°C), since it is austral winter and the water sources are the EACC and the NEMC (Figure 11a, middle row). The uniformly cold temperature is only

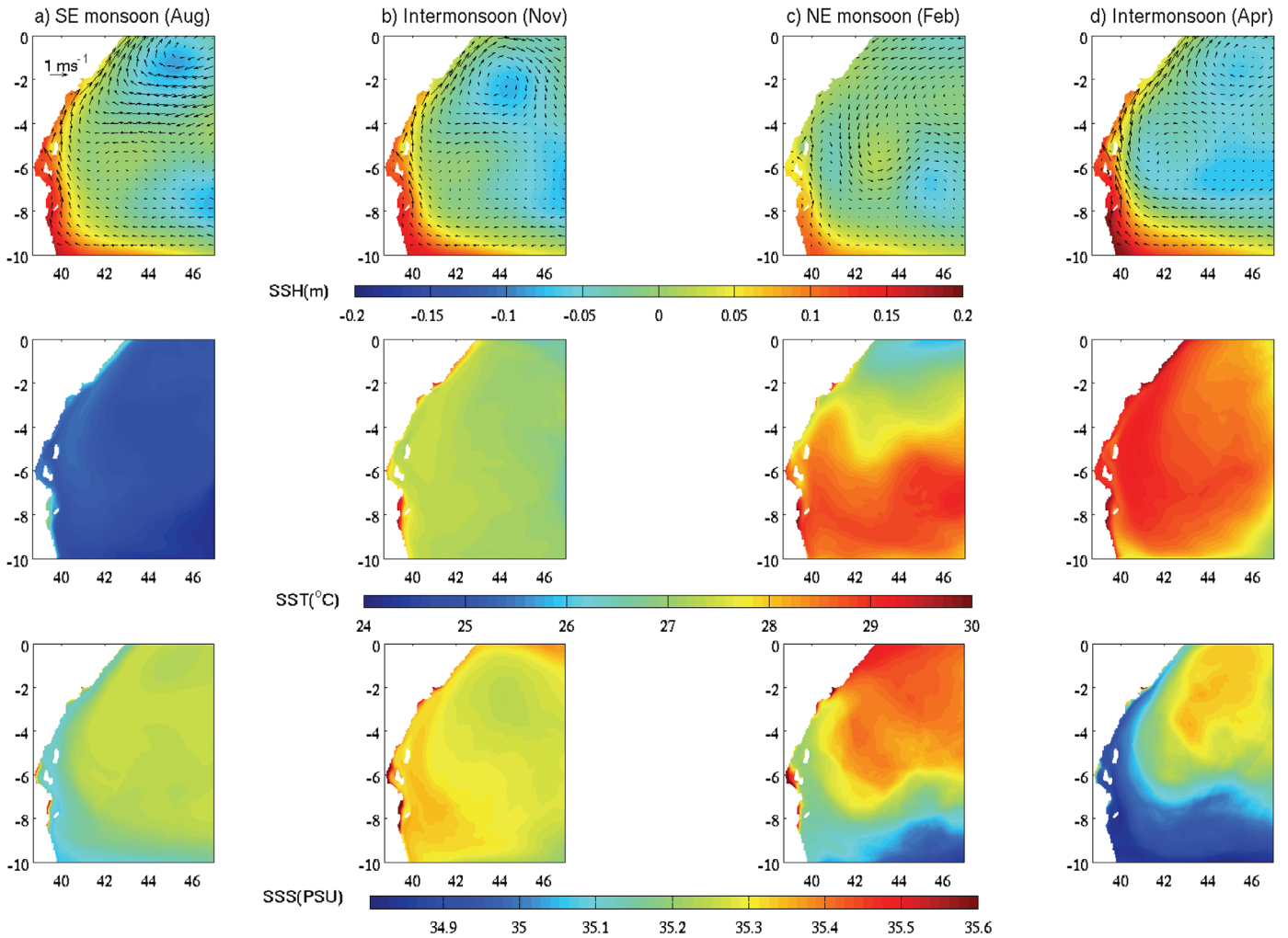

Figure 11. KTCM climatological monthly means representative of the seasonality of the modeled region: (top row) modeled SSH (m) with surface velocity vectors overlaid, (middle row) modeled SST (°C), and (bottom row) modeled SSS (PSU).

observed from July to September, after which warming begins. Low sea surface salinity (SSS $<$ 35.3 PSU) characteristic of the EACC is observed next to the coast during this period. The lowest SSS values are found along the shelf and in the band south of 9°S (Figure 11a, bottom row) from May to July. The partial representation of the Southern Gyre during August has an intermediate salinity of $<$35.2 PSU, in agreement with observations reported by *Schott and McCreary* [2001].

3.2.2. Intermonsoon (November)

The intermonsoon that follows the strong SE monsoon is illustrated by November. It has weaker surface velocities in the offshore region, especially away from the Southern Gyre which is now fully inside the domain (Figure 11b, top row). The offshore extent of the EACC core at the surface ($>$80 cm s^{-1}) is much more coastal restricted, with northward flow again restricted to the upper 400 m (Figure 12b). The southward flowing Somali Current meets the EACC north of the equator (outside our domain) in the OFES model. Therefore, the EACC appears continuous through the KTCM domain, with an offshore jet at the northern boundary that supplies the SECC. SST increases to $>$27°C in the entire interior domain (Figure 11b, middle row). The warmest and saltiest surface water occurs on the shelf where velocities are lower (e.g., with long residence time) and solar heating and evaporation are stronger. The lower salinity signature of the Southern Gyre is evident in the northern half of the domain (Figure 11b, bottom row).

3.2.3. Northeast Monsoon (December–March)

During the NE monsoon from December to March, the northward flowing EACC and the southward flowing SC meet inside the domain (at approximately 0°–3°S). The SC flows southward in the upper ~60 m; below

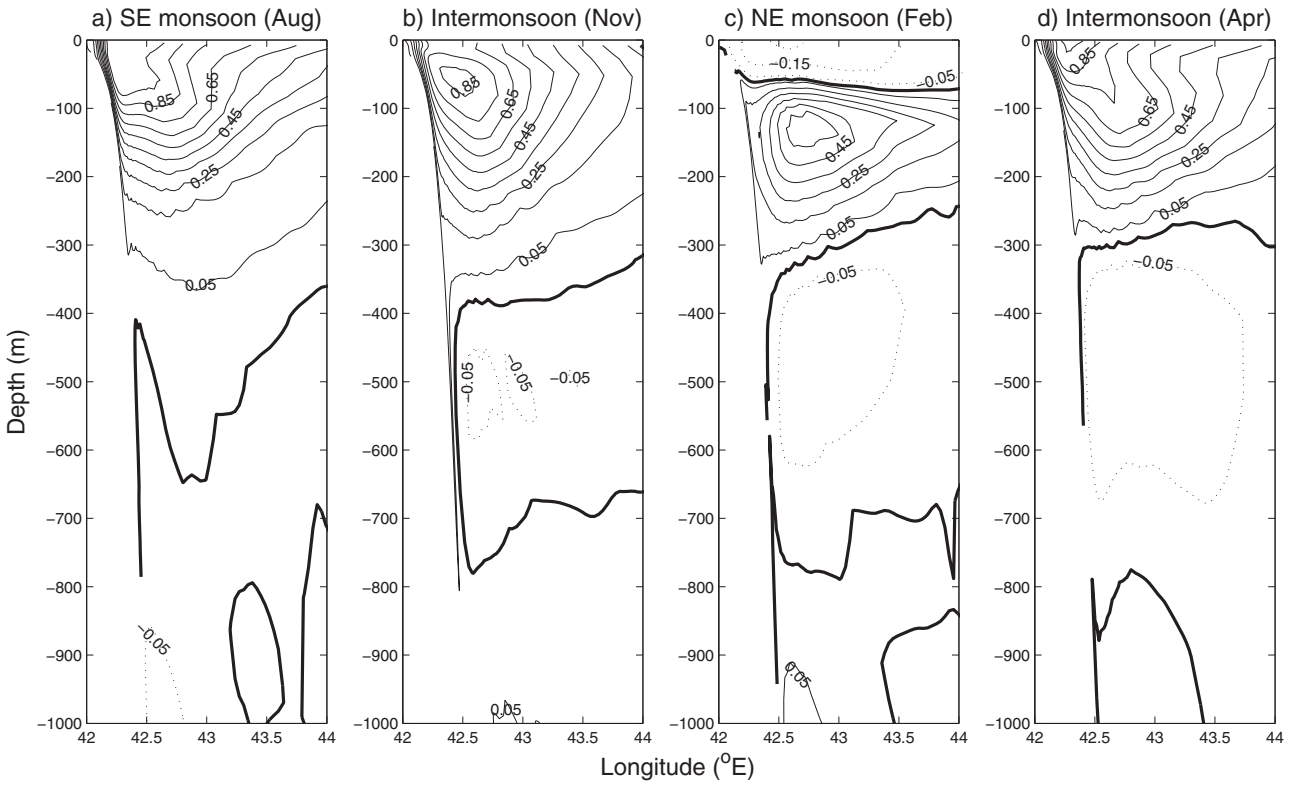

Figure 12. North-south (v) velocity (m s^{-1}) at 1°S. Marked isotachs have a 10 cm s^{-1} interval, starting from ±5 cm s^{-1}; the solid thick line is zero velocity; thin solid lines mark northward velocity contours; and dashed lines show southward velocity contours.

it, the EACC continues to flow northward but lacks a surface expression. Thus, there is a strong vertical shear at ~70–80 m depth (Figure 12c). The latitude where the currents meet progressively shifts southward from the equator in December to ~3°S in March. Where the currents meet, an offshore jet forms the SECC. It flows directly eastward in December but rotates southward through time until it is aligned toward the south in February. A dipole is associated with the SECC jet, with an anticyclonic eddy to its north/east side and a cyclonic eddy (the former SG) to its south/west side. The dipole moves onshore and southward, and by March the cyclonic eddy is compressed against the coast. The dipole is fully inside the domain from January to March. The interaction of these eddies determines the location (latitude) of SECC outflow at the eastern boundary of the domain. The offshore position of the SECC jet at 47°E (our eastern model boundary) shifts southward from the equator in November to 4°–6°S in January–March (Figure 11c, top row). A strong north-south SST difference (of up to 3°C) is observed during the NE monsoon. Warm fresher water is advected into the domain from the south by the EACC, while the SC brings cold saltier water from the northern hemisphere (where strong coastal upwelling is occurring) (Figure 11c, middle and bottom rows). The "cold" surface water feature extends to the confluence of the currents on the shelf (0° in December to approximately 3°–4°S in February).

3.2.4 Intermonsoon (April)

In April, the southward flow of the Somali Current weakens and the continuous northward flow is reestablished along the northern region of the East African coast. The EACC becomes once again a surface current (Figure 12d). The dipole and offshore jet that contributed to the SECC during the NE monsoon period disappear. Highest offshore velocities are now found in the westward flows at 7°–10°S as the SEC feeding the NEMC strengthens (Figure 11d, top row). The transition of the SST pattern from the NE monsoon to the SE monsoon condition is slower than the transition for the circulation and spans over 3 months (April–June). This transition is also slower than the one observed during the SE to NE intermonsoon season (November). In April, as the inflow of the SC stops, SST in most of the domain warms to 29°C (Figure 11d, middle row). In May, the warm water is pushed toward the coast, as colder water advects into the domain through the southern and eastern open boundaries. By June, the warm water (>28°C) has been flushed out through the

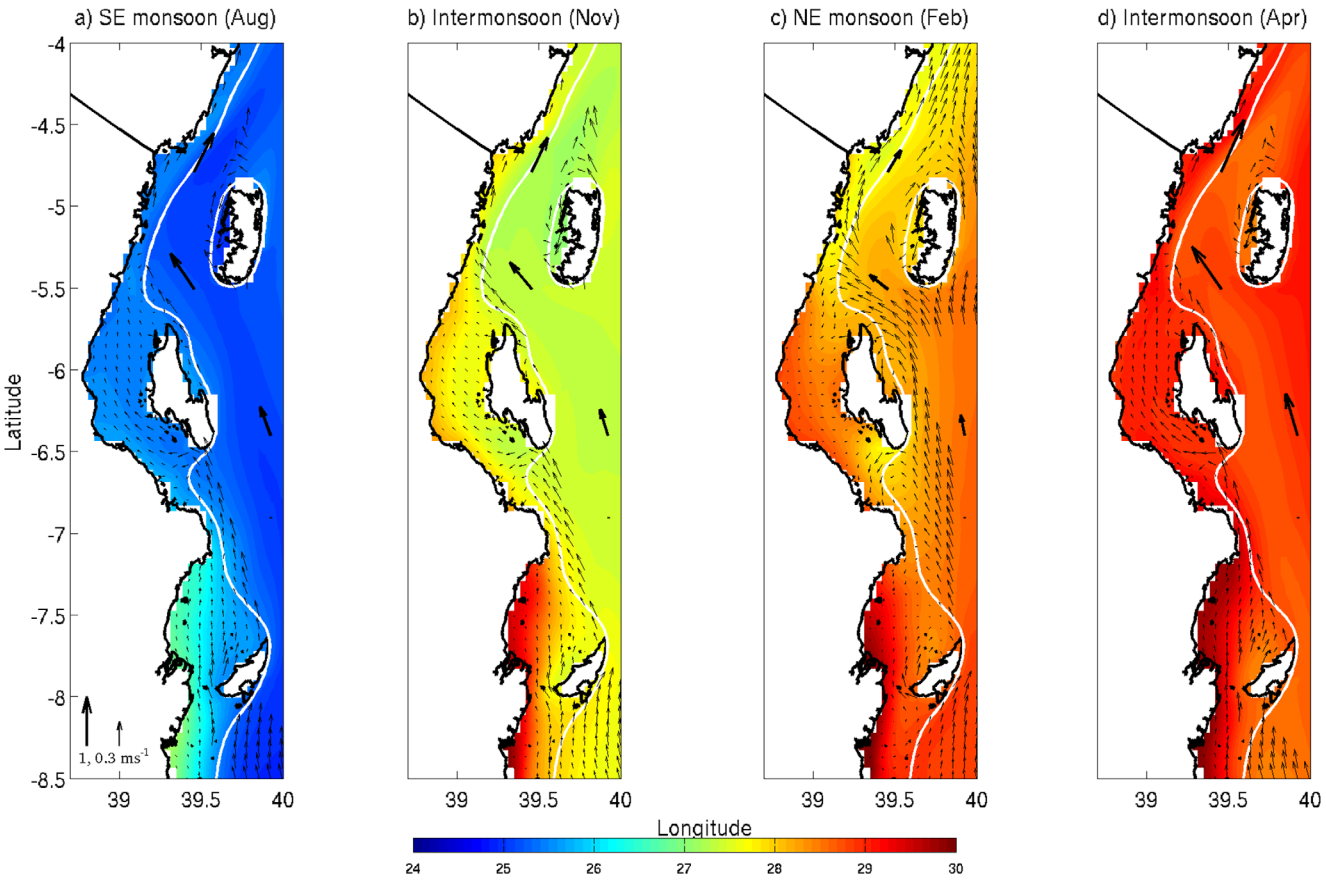

Figure 13. SST with surface velocity vectors overlaid for the Tanzanian shelf region. The islands from north to south are Pemba, Zanzibar, and Mafia. For clarity, only every third vector is shown and vectors with a speed greater than 0.4 m s^{-1} were removed. Thick arrows show strong currents representing the removed vectors. Scale arrows in the left apply to all figures. White contour is the 100 m isobath.

northern open boundary by the EACC. The greatest salinity gradient is observed in April, with fresher water (34.8 PSU) along the southern boundary of the domain and saltier water (35.4 PSU) in the NE corner (Figure 11d, bottom row). Fresher water extends along the shelf all the way to the northern boundary, showing the coastal influence of the EACC on the shelf water mass as well as the influence of local precipitation, which has an annual maximum in May.

3.3. Seasonal Variability of Shelf Circulation

As geostrophic currents approach the shelf, inshore of the 1000 m isobath, they accelerate due to conservation of volume and are deflected to follow lines of constant potential vorticity (here, constant depth). Inshore of the 100 m isobath, currents slow due to friction, the blocking effect of islands, and the barrier that shallow bathymetry represents to deep flows. Between 4° and 8.5°S the larger-scale EACC flows northward year round. The effect of the three large islands on the coastal circulation depends on the intensity of the EACC, the depth of the channels between the islands and the mainland (Pemba >100 m; Zanzibar and Mafia <40 m) and the coastline geometry. Therefore, the circulation patterns around the islands vary both temporally and spatially along the Kenyan-Tanzanian shelf (Figure 13). The coastal region is where higher resolution models, such as KTCM, enable a detailed look at the circulation, which is not well resolved by coarser resolution models.

During the SE monsoon and the two intermonsoon periods (throughout April–November, Figures 13a, 13b, and 13d), the EACC is strong (>85 cm s^{-1}). Shelf flows are northward all along the coast, both inside and outside the channels since the EACC is able to overcome the obstacles that the shallow channels represent. During the NE monsoon (December–March, Figure 13c), the EACC is slower (<75 cm s^{-1}) and the shallow channels inshore of Mafia and Zanzibar Islands impede the northward flow, while channel flow inshore of

Pemba continues. Shelf flow at the southern entrances of the channels differs among the islands during this period, since it depends on channel depth and coastline morphology.

Friction with the coast causes an across-shore gradient of the northward shelf currents. The positive curl in the currents generates small anticyclonic eddies where the coastline morphology allows it: at the southern tips of the islands, to the north of capes and in bays, especially during the NE monsoon when the EACC is slower. The gradient in the current velocities and conservation of potential vorticity causes a small portion of the northward flowing EACC to turn southward into the northern entrance of channels after it passes east of the islands. This return flow is minimal at the northern tip of Pemba Island but persistent year round, while to the north of Zanzibar Island it is strongest from December to March (NE monsoon). The cape near Dar Es Salaam (~7°S) generates a permanent anticyclone in the southern entrance of the Zanzibar Channel that partially impedes the flow through the channel year round. The concave shape of the east coast of Zanzibar Island has a similar effect, which establishes a permanent anticyclonic eddy at 6°S, 39.5°E (Figure 13). Anticyclonic eddies are also present in Unguana Bay and at the south entrance of the Mafia Channel but only when offshore velocities are less than 70 cm s^{-1} (i.e., from December to March).

From November to March, the anticyclonic eddy in the southern entrance of the Zanzibar Channel blocks most of the slow flowing EACC. The small northward flow that enters the Zanzibar Channel from the south meets the return flow coming from the north, creating sluggish circulation inside the channel (<20 cm s^{-1}, Figures 13 and 14). The waters of the Zanzibar Channel are nearly isolated during this period. In April, offshore EACC speeds reach 1 m s^{-1} and northward along channel speeds increase to 28 cm s^{-1}, the southward return flow in the Zanzibar Channel is restricted to the region near the northern entrance. In May, as its speed increases, the EACC is able to force itself into the southern entrance of the Zanzibar Channel despite the blockage of the anticyclonic eddy, and northward flow through the Zanzibar Channel is reestablished with velocities along the channel of up to 39 cm s^{-1}. The Mafia Channel is similar in depth to the Zanzibar Channel, and despite being narrower on its southern entrance, the northward flow through the channel is only completely blocked during January and partially blocked during December and February, since the eddy at its southern entrance is weaker and restricted to the upper ~10 m. The much deeper (>100 m) Pemba Channel allows the EACC to continue northward through it all year round (Figure 13).

Several processes are responsible for the east-west gradients of temperature in the region inshore of the three islands from November to February (Figures 13b and 13c). The less intense circulation on the continental shelf allows temperatures in the shallow regions to evolve differently than in the rest of the domain. In November, when currents relax the narrow shelf warms quickly until it starts being affected by the cooler SC in the north (Figures 11b and 11c, middle row). In the deep channel inshore of Pemba, temperature changes are mainly due to advection, which is not seasonally interrupted, and temperatures are more similar to those in the main offshore flows of the EACC. Circulation and water exchange in the Zanzibar Channel are minimal during November–February; this allows the waters in the shallow channel to warm more than those outside the channel. The anticyclone in the southern entrance of the Zanzibar Channel generates localized upwelling of cooler waters next to the southern coast of Zanzibar Island. Although the cooler temperatures next to the island are most evident during November–February (Figures 13b and 13c), analyses of vertical velocities along a transect stretching from the southern coast of the island to the mainland (not shown) reveal positive vertical velocities throughout the water column next to the island in all months, along with downwelling in the core of the anticyclonic eddy, which spans the full depth of the water column (~40 m) and is present in all months. In the narrow region (~10–20 km) next to the mainland coast, local heating warms shallow, sluggish regions, particularly during the onset of the monsoon periods (March–April and November–December) when wind forcing is at its minimum. The shallow bays along the mainland coast north and south of Mafia Island are always warmer than surrounding regions. Cooler SSTs are observed adjacent to the west coast of Mafia Island (Figure 13, i.e., November and February), possibly due to localized upwelling as the northward flow passes around the islands [*Hamner and Hauri*, 1981].

4. Discussion

The interaction of the seasonally reversing SC with the more persistent flow of the EACC creates complex circulation patterns, especially when coupled with strongly seasonal monsoonal winds and the presence of islands with channels of various depths off Kenya and Tanzania. Previous ocean circulation models have not

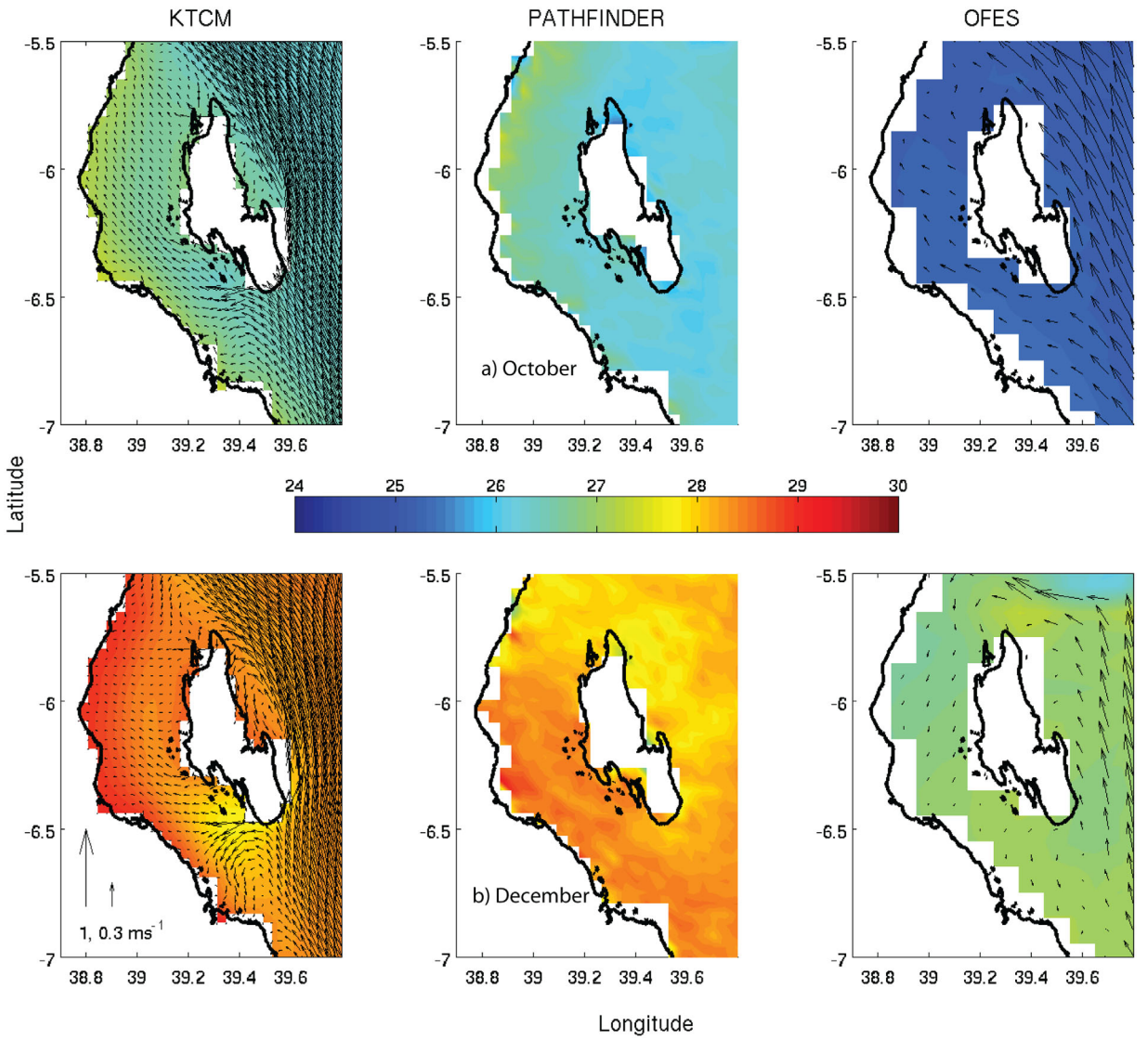

Figure 14. SST around Zanzibar Island is shown in color for (a) October and (b) December, from KTCM, the Pathfinder satellite product and OFES. Velocity vectors are shown at full resolution for both models. Scale arrows in the lower left apply to all figures.

resolved the circulation inshore and around these islands. Our goal in developing the high-resolution KTCM is to better resolve the details of the shelf circulation, while maintaining or improving shelf circulation connections with the broader forced dynamics caused by large-scale wind and remote forcings. The results demonstrate success in achieving these goals with respect to seasonal patterns of surface circulation and water properties, with some caveats that warrant further discussion.

The KTCM SSTs compare well with satellite SST fields and provided regional improvement on the large-scale OFES model SSTs along the western boundary (Figure 4). The KTCM also eliminated the 1–2°C cold bias from the global OFES model (Figures 4 and 14). Below the sea surface, the KTCM adequately hindcasts vertical temperature profiles from the WOD09 from specific locations and times (Figure 9). Temperature hindcasts are least skillful at mid depths (75–250 m), where there is increased temperature variability due to the coarser vertical resolution of the model and, potentially, differences in stratification, mixed layer depths, and isotherm displacements by internal waves (Figure 9). Although the scarcity of in situ salinity data in this region during the modeled time period prevents a thorough assessment of the fidelity of the model salinity, the general subsurface salinity structure agrees with published salinity sections from earlier periods [i.e., *Swallow et al.*, 1991; *Schott and McCreary*, 2001; *Schott et al.*, 2002].

The volume transports in the EACC, the SC, and the offshore jet that contributes to the SECC in the model are seasonally consistent with prior field studies (Figure 11) [*Swallow et al*., 1991; *Schott and McCreary*, 2001; *Reid*, 2003; *Schott et al*., 2009]. Quantitative comparisons with observations of these large-scale features are difficult, due to the lack of observations throughout the annual cycle and the lack of long time series that allow an observation-based climatology. However, the few observations of the magnitude and seasonality of volume transport of these currents suggest consistency of the model and observed transports. Surface circulation is also indicated by fields of sea surface height and the KTCM SSH fields reproduce the dominant statistical mode of SSH variability, as represented by AVISO altimetry. The ability of KTCM to reproduce monthly seasonal fields of SSH is similar to that of OFES. Both the KTCM and 10 km OFES reproduce the satellite fields during months when the SSH fields have strong gradients and relatively simple structure but have difficulty reproducing the SSH patterns when smaller-scale spatial variability is high and horizontal gradients in SSH are weak (Figures 6 and 8).

Direct comparisons of KTCM results to other models of the region are difficult due to differences in model resolution and simulated time. However, as far as the presence and characteristics of the main circulation features and seasonal timing, KTCM broadly agrees with coarser resolution OGCMs of *Lee and Marotzke* [1998] and *Anderson et al*. [1991], an earlier ROMS by *Hermes and Reason* [2008], and the Simple Ocean Data Assimilation (SODA) product evaluated by *Xie et al*. [2002]. Our model compares better to Levitus SST and ship-drift derived currents climatology used by *Mishra et al*. [2007] to evaluate their global Modular Ocean Model (MOM3.0) simulation of the southern Indian Ocean, which does not perform well in our study region. KTCM SST and SSH seasonal cycles compare well to the larger-scale ROMS model of *Manyilizu et al*. [2014]. Their climatological SST for the month of May shows a region of relatively cool surface water north of Madagascar. This is consistent with the April cooling we see in the southeast corner of our model domain (Figure 11 and supporting information). The presence of this cool feature in the middle of Manyilizu's larger model domain confirms that this is not an spurious feature in our model caused by the cold-biased boundary forcing from OFES and verifies that the influence of the open boundary forcing on SST is restricted to regions less than 200 km wide around the perimeter of our model domain.

We did not find evidence in the Kenya and Tanzania region of a strong local influence of the zonal wind stress as was suggested by *Pandey and Rai* [2008] for the coastal regions of the tropical Indian Ocean north of 5°S. They use a basin-scale Princeton Ocean Model (POM) with 5′ resolution topography and no islands to discuss the large-scale coastal circulation. Based on a 1/6° resolution ROMS model of the tropical western Indian Ocean, *Manyilizu et al*. [2014] report that SST interannual variability in a region off southern Tanzania (40°–42°E and 8°–10°S) is weak in comparison to an offshore region and predominantly driven by surface heat flux. Their analysis focuses only on SST and does not investigate circulation patterns which are the main focus of our study. In the KTCM, the prevalence of northward flow along the coast south of 5°S during January and February (Figures 11, top row and 13), when the local wind is blowing southward (Figure 3) appears counterintuitive. In fact, it highlights the importance of large-scale remote forcing on the regional circulation. In this case, the southern hemisphere EACC opposes the northern hemisphere NE monsoonal winds, which cause the reversal of the Somali Current. The strong northern hemisphere winds and the southward equator crossing strong flows that result are the main influences over the modeled region, overpowering the effects of local winds on the circulation. However, neither diurnal variability in the wind forcing nor freshwater runoff is included in the KTCM, and either or both might influence coastal circulation. These forcings should be included in future model studies.

As intended, the KTCM significantly increases the spatial resolution of the circulation around the islands (e.g., Figures 13 and 14). The coastal circulation patterns of the KTCM are likely to be more realistic than those of the OFES since bathymetry is represented more accurately, allowing nonlinear interactions between the flow and the bottom topography to be better resolved. However, coastal ocean observations off East Africa are too sparse to reliably validate nearshore coastal model results with observations. Without better velocity and hydrographic observations on the shelf, it is not possible to quantitatively assess the improvement provided by the KTCM. Thus, we present these patterns as working hypotheses, which could be verified by in situ observations, such as water temperature observations reported recently for a location in the Zanzibar Channel (Chumbe Island Coral Park) by *Manyilizu et al*. [2014]. The KTCM near-bottom temperature agrees well with the in situ temperature from loggers at Chumbe Island Coral Park (Figure 15). Thus, we have confidence that KTCM is reproducing well temperatures observed at one site in the Zanzibar Channel for which observations exist during our model time period.

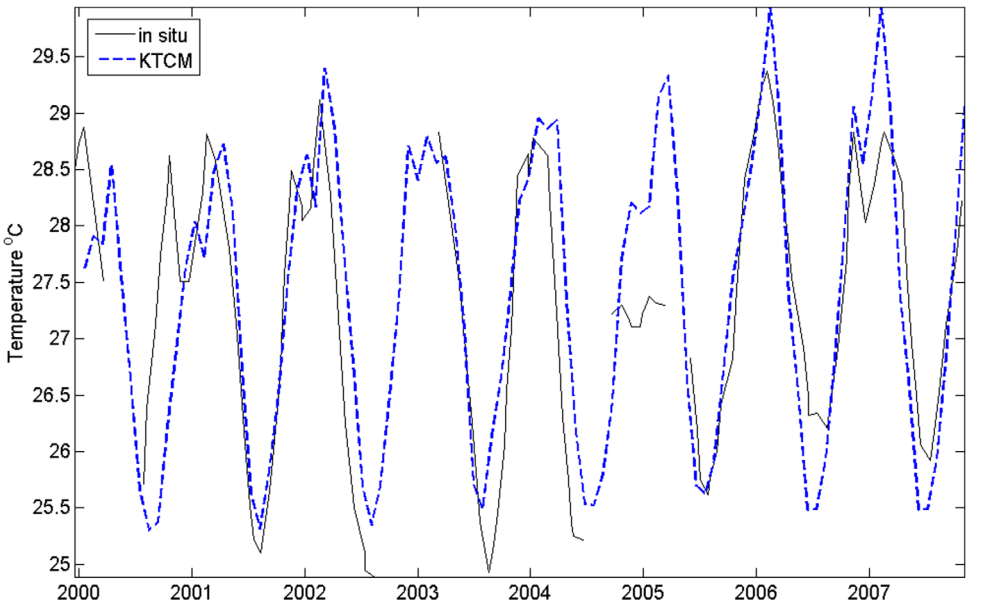

Figure 15. In situ near-bottom temperatures at Chumbe Island Coral Park in the Zanzibar Channel reported in *Manyilizu et al.* [2014] (black line) and concurrent temperature from the KTCM (blue dashed line).

While the KTCM better represents satellite SST compared to OFES over the broader model domain, the small-scale spatial SST patterns within the channels are not always in agreement with satellite observations. Figure 14 provides an example of this for the region surrounding Zanzibar Island. In October, when there is continuous northward flow through the Zanzibar Channel, both Pathfinder and KTCM show a small SST gradient inshore and offshore of the island with slightly warmer SST inshore, whereas the coarser resolution OFES shows uniformly colder SST (Figure 14, top row). In December, when the circulation into the Zanzibar Channel in KTCM is largely blocked by eddies at both channel ends, Pathfinder shows stronger SST gradients with warmer water in the southern channel. KTCM, however, shows cooler (warmer) water in the southern (northern) Zanzibar Channel. The gradients in OFES are minimal (Figure 14, bottom row). The SST patterns in KTCM show localized upwelling of cooler water SW of the island, while westward flow of this cooler water displaces the warm surface water to the NW. As described above, the upwelling is present in all months, although its surface signature depends on stratification. Further studies at smaller spatial and temporal scales are needed to determine the skill of KTCM to reproduce the small-scale SST and circulation patterns and to assess biases in both satellite and model fields. Problems with infrared satellite SST retrievals are well known. Surface warming during calm periods produces warm and very thin skin layers that mask the more representative upper ocean temperatures beneath those layers. Atmospheric correction algorithms may also be in error due to small clouds and humid tropical conditions. These may keep the Pathfinder field in December from seeing the results of upwelling. Important sources of variability not included in the model like freshwater runoff and diurnal wind variability may modify the circulation pattern and SST, particularly in shallower coastal regions. Measurements of temperature, salinity, and current velocities at higher spatial and temporal scales are crucial to corroborate nearshore circulation patterns and hydrography, especially in heterogeneous systems, where very local processes, such as small-scale upwelling may be important.

Coastal regions of Kenya and Tanzania depend heavily on their coastal resources for a variety of ecosystem services. The resources are vulnerable to both global and local anthropogenic stressors. Global stressors include excessive carbon dioxide emissions leading to global warming, sea level rise, water temperature increases, and ocean acidification. Local stressors include pollution and overfishing. Understanding coastal physical processes at the local scale and having local-scale physical models of ocean circulation and hydrography are valuable for investigating the impacts of anthropogenic stressors in coastal systems and can help design strategies to mitigate their negative effects. For example, one of the primary findings of the KTCM simulation is the presence of a bimodal coastal circulation, with strong northward flow through the

channels inshore of the islands during most of the year but restricted channel throughflow inshore of Mafia and Zanzibar Islands during the northeast monsoon (December–March). Preliminary Lagrangian particle tracking experiments [*Mayorga-Adame*, 2010] show that the strong northward flow during March–November implies shorter residence times of the water in the Zanzibar and Mafia Channels compared to the sluggish shelf circulation during the NE monsoon (December–February). This has important implications for ecological issues such as nearshore pollutant dispersal, mariculture operations, coral reef health, and the connectivity of coral reef organisms. Strong coastal flows are beneficial for coral reef health and mariculture operations since they constantly supply oxygenated, nutrient rich water to the organisms. They are also locally beneficial in reducing pollutant concentrations near their source due to rapid flushing, enhanced dispersion and strong mixing. Wide dispersal of pollutants during the strong flow regime will impact larger regions, including significant marine habitats such as mangroves and coral reefs. However, lower concentrations of pollutants in a larger area generally have lower negative effects on an ecosystem than higher pollutant concentrations in a smaller area [*Pastorok and Bilyard*, 1985], as would occur during the sluggish circulation regime. Slow flows promote retention which may benefit recruitment of coral reef associated species that need to find suitable habitat at the end of their pelagic larval phases. Rapid flows may imply losses for local populations but enhance one way connectivity between southern and northern reefs and increase the probability of colonizing new habitat [*Sammarco and Andrews*, 1988; *Cowen and Sponaugle*, 2009].

For regions with limited observing capacity, such as East Africa, regional ocean circulation models like the KTCM offer a wide range of possibilities for examining physical phenomena despite a lack of in situ physical observations and provide opportunities for advancing our understanding of the regional ocean circulation and its effects on marine ecosystems. The hindcast ability of the KTCM could be used to address the effects of global climate changes on ocean circulation and environmental issues along the East African coast including sea level rise, coastal erosion, dispersion of pollutants, coral stress due to extreme temperatures, coral reef connectivity, and the potential spillover effect of harvested and ecologically important species beyond the boundaries of Marine Protected Areas. KTCM can provide the velocity and temperature fields required by individual based biological models and other process-oriented models to test hypotheses about environmental stresses and ecological issues of the Kenyan-Tanzanian coastal region. Model simulations can also guide cost effective in situ observation campaigns to maximize available resources.

5. Summary

1. This paper presents results of the Kenya-Tanzania Coastal Model (KTCM), a 4 km horizontal resolution ROMS application (Figure 1), forced locally by daily atmospheric fields from NCEP/NCAR reanalysis and remotely at the open boundaries by hydrography, SSH and velocity fields from the global model OFES and OTPX tidal forcing.
2. The KTCM's SST compares well with Pathfinder satellite observations improving the SST representation provided by the parent model OFES which has a cold bias (Figure 4). Pathfinder SST seasonal and interannual variability is also adequately reproduced by our model (Figure 5).
3. The climatological circulation patterns of the KTCM reproduce the main features reported for the region by previous observational and modeling studies. The KTCM SSH fields reproduce the dominant statistical mode of SSH variability, as represented by AVISO altimetry, which is indicative of the observed surface circulation.
4. A comparison to WOD09 temperature profiles shows that the model adequately hindcasts subsurface temperatures seasonally and spatially. Larger differences are observed at the main thermocline depth, where variability is expected to be high and the model has coarser resolution (Figure 9). Due to the sparsity of salinity observations, model results were only qualitatively compared with a vertical salinity section reported in the literature. The main observed features are represented in the model climatology (Figure 10).
5. KTCM adequately reproduces the main mesoscale features described for the region, while greatly increasing the details of the coastal circulation and hydrography in comparison to previous modeling and observational studies. We provide a climatological estimate of the seasonality of the ocean state based on an 8 year simulation of a dynamically coherent model (Figure 14). This provides a working hypothesis for the seasonal coastal circulation in a region that lacks long-term observations needed to define a reliable representation of the ocean on a typical year.

6. The KTCM monthly climatological fields (Figure 14) describe the circulation. *SW monsoon conditions*: strong continuous northward flow along the coast of the modeled domain and "cool" (~24°C) SST prevails from May to October. *Intermonsoon conditions*: weakening of the EACC and surface velocities in the offshore region, with SST warming in November. *NE monsoon conditions*: from January to March, a strong north-south SST gradient is caused by the intrusion of the shallow, southward flowing, cold and salty Somali Current that meets the slow northward flowing, warm and fresh EACC. The convergence of the two currents forms the eastward flowing SECC. *Intermonsoon conditions*: the transition back to SW monsoon conditions occurs in April, with slow SST cooling and the reestablishment of northward flow all along the coast with the strengthening of the EACC.
7. The detailed shelf circulation consists of a bimodal coastal circulation pattern, with strong northward flow through the channels inshore of the islands during most of the year, but restricted channel throughflow inshore of Mafia and Zanzibar Islands during the northeast monsoon (December–March) (Figures 13 and 14).
8. This modeling study provides some guidance for future work. The shelf circulation patterns and hydrography of KTCM include a more accurate and detailed bathymetry but do not include diurnal wind variability and local fresh water runoff. These should be included in future studies. At fine scales the KTCM SST fields on the shelf do not always agree with Pathfinder satellite observations (Figure 14), which may be affected by a warm surface skin and errors in the atmospheric corrections due to small clouds and the humid tropical atmosphere. Concurrent direct measurements and satellite observations are needed to evaluate this further.
9. Implications of the shelf circulation patterns on various environmental issues affecting the Kanyan-Tanzanian coastal region are briefly discussed.

Acknowledgments

Support for C.G.M.A. was provided by Fulbright-Garcia Robles scholarships of the Comision Mexico-Estados Unidos (COMEXUS), Consejo Nacional de Ciencia y Tecnologia (CONACYT), and NSF grant OCE-0630471. Support for P.T.S. was provided by NSF grant OCE-0815007, NASA grant NNX08AR40G, NASA grant NNX13AH22G, and NOAA grant NA08NES4400013. Support for H.P.B. was provided by NSF grant OCE-0816358. OFES data were provided by Manu DiLorenzo (edl@eas.gatech.edu) at Georgia Institute of Technology with assistance from Vincent Combes at the College of Ocean and Atmospheric Sciences of Oregon State University. Yohanna Shaghude (shaghude@ims.udsm.ac.tz) at the Institute of Marine Sciences of the University of Dar Es Salaam provided digitized nautical charts of the region and depth measurements collected with sounders. All other data used to develop and validate KTCM are freely available from URLs: NCEP/NCAR atmospheric variables (http://www.esrl.noaa.gov/psd/data/gridded/data.ncep.reanalysis.html), Pathfinder v5 satellite SST (http://www.nodc.noaa.gov/sog/pathfinder4km/), SLA fields from AVISO (http://www.aviso.altimetry.fr/), WOD09 temperature profiles (https://www.nodc.noaa.gov/OC5/WOD09/pr_wod09.html), ETOPO-2 bathymetry data (http://www.ngdc.noaa.gov/mgg/global/relief/ETOPO2/ETOPO2v2-2006/), TPXO-8 tidal solution for the Indian Ocean (http://volkov.oce.orst.edu/tides/atlas.html), the ROMS code can be downloaded upon registration at (http://volkov.oce.orst.edu/tides/atlas.html). All application specific input data files and results produced by the KTCM are available from the corresponding author upon request (cmayorga@coas.oregonstate.edu).

References

Anderson, D. L. T., D. J. Carrington, R. Corry, and C. Gordon (1991), Modeling the variability of the Somali current, *J. Mar. Res.*, *49*(4), 659–696.

Barale, V., J. F. R. Gower, and L. Alberotanza (Eds.) (2010), *Oceanography from Space Revisited*, Springer, N. Y., doi:10.1007/978-90-481-8681-5.

Beckmann, A., and D. B. Haidvogel (1993), Numerical simulation of flow around a tall isolated seamount. Part I: Problem formulation and model accuracy, *J. Phys. Oceanogr.*, *23*, 1736–1753.

Bendekovic, J., and D. Vuletic (2013), Piracy influence on the shipowners and insurance companies, in *DAAAM International Scientific Book*, edited by B. Katalinic and Z. Tekic, chap. 42, pp. 711–718, DAAAM Int., Vienna, doi:10.2507/daaam.scibook.2013.42.

Chassignet, E. P., H. E. Hurlburt, O. M. Smedstad, G. R. Halliwell, P. J. Hogan, A. J. Wallcraft, R. Barailled, and R. Bleck (2007), The HYCOM (HYbrid Coordinate Ocean Model) data assimilative system, *J. Mar. Syst.*, *65*(1), 60–83.

Collins, C., C. J. C. Reason, and J. C. Hermes (2012), Scatterometer and reanalysis wind products over the western tropical Indian Ocean, *J. Geophys. Res.*, *117*, C03045, doi:10.1029/2011JC007531.

Cowen, R. K., and S. Sponaugle (2009), Larval dispersal and marine population connectivity, *Annu. Rev. Mar. Sci.*, *1*, 443–466.

Cowen, R. K., C. B. Paris, and A. Srinivasan (2006), Scaling of connectivity in marine populations, *Science*, *311*(5760), 522–527.

da Silva, J. C. B., A. L. New, and J. M. Magalhaes (2009), Internal solitary waves in the Mozambique Channel: Observations and interpretation, *J. Geophys. Res.*, *114*, C05001, doi:10.1029/2008JC005125.

Egbert, G. D., and S. Y. Erofeeva (2002), Efficient inverse modeling of barotropic ocean tides, *J. Atmos. Oceanic Technol.*, *19*(2), 183–204.

Egbert, G. D., A. F. Bennett, and M. G. G. Foreman (1994), TOPEX/POSEIDON tides estimated using a global inverse model, *J. Geophys. Res.*, *99*(C12), 24,821–24,852.

Fieux, M (2001), Somali current, in *Encyclopedia of Ocean Sciences*, edited by J. H. Steele et al., pp. 2839–2849, Academic, San Diego, Calif.

Fieux, M., and G. Reverdin (2001), Current systems in the Indian Ocean, in *Encyclopedia of Ocean Sciences*, edited by J. H. Steele et al., pp. 598–604, Academic, San Diego, Calif.

Gommenginger, C., P. Thibaut, L. Fenoglio-Marc, G. Quartly, X. Deng, J. Gómez-Enri, P. Challenor, and Y. Gao (2011), Retracking altimeter waveforms near the coasts, in *Coastal Altimetry*, edited by S. Vignudelli et al., pp. 61–101, Springer, Berlin.

Haidvogel, D. B., et al. (2008), Ocean forecasting in terrain-following coordinates: Formulation and skill assessment of the Regional Ocean Modeling System, *J. Comput. Phys.*, *227*(7), 3595–3624.

Hamner, W. M., and I. R. Hauri (1981), Effects of island mass—Water-flow and plankton pattern around a reef in the Great Barrier-Reef lagoon, Australia, *Limnol. Oceanogr.*, *26*(6), 1084–1102.

Hermes, J. C., and C. J. C. Reason (2008), Annual cycle of the South Indian Ocean (Seychelles-Chagos) thermocline ridge in a regional ocean model, *J. Geophys. Res.*, *113*, C04035, doi:10.1029/2007JC004363.

Jerlov, N. G. (1976), *Marine Optics*, 247 pp., Elsevier, Amsterdam (Elsevier oceanography series).

Kalnay, E., et al. (1996), The NCEP/NCAR 40-year reanalysis project, *Bull. Am. Meteorol. Soc.*, *77*(3), 437–471.

Lee, T., and J. Marotzke (1998), Seasonal cycles of meridional overturning and heat transport of the Indian Ocean, *J. Phys. Oceanogr.*, *28*(5), 923–943.

Manyilizu, M., F. Dufois, P. Penven, and C. Reason (2014), Interannual variability of sea surface temperature and circulation in the tropical western Indian Ocean. *Afr. J. Mar. Sci.*, *36*(2), 233–252, doi:10.2989/1814232X.2014.928651.

Marchesiello, P., J. C. McWilliams, and A. Shchepetkin (2001), Open boundary conditions for long-term integration of regional oceanic models, *Ocean Modell.*, *3*(1–2), 1–20, doi:10.1016/S1463-5003(00)00013-5.

Martin, S. (2014), *An Introduction to Ocean Remote Sensing*, Cambridge Univ. Press, 426 pp., Cambridge, U. K.

Matano, R. P., E. J. Beier, P. T. Strub, and R. Tokmakian (2002), Large-scale forcing of the Agulhas variability: The seasonal cycle, *J. Phys. Oceanogr.*, *32*(4), 1228–1241.

Matano, R. P., E. J. Beier, and P. T. Strub (2008), The seasonal variability of the circulation in the South Indian Ocean: Model and observations, *J. Mar. Syst.*, *74*(1–2), 315–328.

Mayorga-Adame, C. G. (2007), Ocean circulation of the Zanzibar Channel: A modeling approach, Outreach program final report, 8 pp., Theiss Res., La Jolla, Calif.
Mayorga-Adame, C. G. (2010), Development, performance evaluation and application of a physical model of the Kenyan-Tanzanian coastal region, MS thesis, 121 pp., Coll. of Ocean and Atmos. Sci., Oreg. State Univ., Corvallis.
Mellor, G. L., and T. Yamada (1982), Development of a turbulence closure model for geophysical fluid problems, *Rev. Geophys. Space Phys.*, *20*, 851–875.
Mishra, A. P., S. Rai, and A. C. Pandey (2007), Ocean model simulation of Southern Indian Ocean surface currents, *Mar. Geod.*, *30*(4), 345–354.
Nauw, J. J., H. M. van Aken, A. Webb, J. R. E. Lutjeharms, and W. P. M. de Ruijter (2008), Observations of the southern East Madagascar Current and undercurrent and countercurrent system, *J. Geophys. Res.*, *113*, C08006, doi:10.1029/2007JC004639.
Odido, M., and S. Mazzilli (Eds.) (2009), *African Oceans and Coasts, IOC Information Document*, 1255 pp., UNESCO-IOC Reg. Bur. for Sci. and Technol., Nairobi, Kenya.
Pandey, A. C., and S. Rai (2008), Sensitivity of the Indian Ocean circulation to surface wind stress, *Indian J. Mar. Sci.*, *37*(1), 55–61.
Pastorok, R. A., and G. R. Bilyard (1985), Effects of sewage pollution on coral-reef communities, *Mar. Ecol. Prog. Ser.*, *21*(1–2), 175–189.
Payet, R., and D. Obura (2004), The negative impacts of human activities in the Eastern African region: An international waters perspective, *Ambio*, *33*(1–2), 24–33.
Reid, J. L. (2003), On the total geostrophic circulation of the Indian Ocean: Flow patterns, tracers, and transports, *Prog. Oceanogr.*, *56*(1), 137–186.
Richmond, M. D. (Ed.) (1997), *Field Guide to the Seashores of Eastern Africa and the Western Indian Ocean Islands*, 448 pp., Swed. Int. Dev. Coop. Agency/Dep. for Res. Coop., Stockholm.
Ridderinkhof, H., P. M. van der Werf, J. E. Ullgren, H. M. van Aken, P. J. van Leeuwen, and W. P. M. de Ruijter (2010), Seasonal and interannual variability in the Mozambique Channel from moored current observations, *J. Geophys. Res.*, *115*, C06010, doi:10.1029/2009JC005619.
Roman, R. E., and J. R. E. Lutjeharms (2009), Red Sea Intermediate Water in the source regions of the Agulhas Current, *Deep Sea Res., Part I*, *56*(6), 939–962.
Sammarco, P. W., and J. C. Andrews (1988), Localized dispersal and recruitment in Great Barrier-Reef corals—The helix experiment, *Science*, *239*(4846), 1422–1424.
Sasaki, H., Y. Sasai, M. Nonaka, Y. Masumoto, and S. Kawahara (2006), An eddy-resolving simulation of the quasi-global ocean driven by satellite-observed wind field, *J. Earth Simulator*, *6*, 35–49.
Schott, F., J. C. Swallow, and M. Fieux (1990), The Somali Current at the Equator—Annual cycle of currents and transports in the upper 1000-m and connection to neighboring latitudes, *Deep Sea Res., Part A*, *37*(12), 1825–1848.
Schott, F. A., and J. P. McCreary (2001), The monsoon circulation of the Indian Ocean, *Prog. Oceanogr.*, *51*(1), 1–123.
Schott, F. A., M. Dengler, and R. Schoenefeldt (2002), The shallow overturning circulation of the Indian Ocean, *Prog. Oceanogr.*, *53*(1), 57–103.
Schott, F. A., S. P. Xie, and J. P. McCreary Jr. (2009), Indian Ocean circulation and climate variability, *Rev. Geophys.*, *47*, RG1002, doi:10.1029/2007RG000245.
Schultz, E. T., and R. K. Cowen (1994), Recruitment of coral-reef fishes to Bermuda—Local retention or long-distance transport, *Mar. Ecol. Prog. Ser.*, *109*(1), 15–28.
Shaghude, Y. W., K. O. Wannas, and S. B. Mahongo (2002), Biogenic assemblage and hydrodynamic settings of the tidally dominated reef platform sediments of the Zanzibar channel, *West. Indian Ocean J. Mar. Sci.*, *1*(2), 107–116.
Smith, S. L., L. A. Codispoti, J. M. Morrison, and R. T. Barber (1998), The 1994–1996 Arabian Sea Expedition: An integrated, interdisciplinary investigation of the response of the northwestern Indian Ocean to monsoonal forcing, *Deep Sea Res., Part II*, *45*(10–11), 1905–1915.
Swallow, J. C., F. Schott, and M. Fieux (1991), Structure and transport of the East-African Coastal Current, *J. Geophys. Res.*, *96*(C12), 22,245–22,257.
Taylor, K. E. (2001), Summarizing multiple aspects of model performance in a single diagram, *J. Geophys. Res.*, *106*(D7), 7183–7192.
Umlauf, L., and H. Burchard (2003), A generic length-scale equation for geophysical turbulence models, *J. Mar. Res.*, *61*, 235–265.
van der Werf, P. M., P. J. van Leeuwen, H. Ridderinkhof, and W. P. M. de Ruijter (2010), Comparison between observations and models of the Mozambique Channel transport: Seasonal cycle and eddy frequencies, *J. Geophys. Res.*, *115*, C02002, doi:10.1029/2009JC005633.
van Katwijk, M. M., N. F. Meier, R. Vanloon, E. M. Vanhove, W. Giesen, G. Vandervelde, and C. Denhartog (1993), Sabaki River sediment load and coral stress—Correlation between sediments and condition of the Malindi-Watamu reefs in Kenya (Indian-Ocean), *Mar. Biol.*, *117*(4), 675–683.
Vimal Kumar, K. G., P. K. Dinesh Kumar, B. R. Smitha, H. Habeeb Rahman, J. Josia, K. R. Muraleedharan, V. N. Sanjeevan, and C. T. Achuthankutty (2008), Hydrographic characterization of southeast Arabian Sea during the wane of southwest monsoon and spring intermonsoon, *Environ. Monit. Assess.*, *140*(1–3), 231–247.
Warner, J. C., C. R. Sherwood, H. G. Arango, and R. P. Signell (2005), Performance of four turbulence closure methods implemented using a generic length scale method, *Ocean Modell.*, *8*, 81–113.
Wyrtki, K. (1973), An equatorial jet in the Indian Ocean, *Science*, *181*, 262–264.
Xie, S. P., H. Annamalai, F. A. Schott, and J. P. McCreary (2002), Structure and mechanisms of South Indian Ocean climate variability, *J. Clim.*, *15*(8), 864–878.